FILAMENTATION INDUCED NONLINEAR OPTICS

Thèse

Shuai Yuan

Doctorat en Physique
Philosophiæ Doctor (Ph. D)

Québec, Canada

Résumé

La filamentation du laser femtoseconde provient d'un équilibre dynamique entre l'autofocalisation Kerr et la défocalisation par le plasma autogénéré produit de l'ionisation multiphotonique/tunnel des molécules dans l'air. Ce phénomène a attiré beaucoup d'attention des scientifiques telles que la télédétection de polluants atmosphériques et l'identification moléculaire par l'alignement des molécules. Cependant, il y a une multitude de processus non linéaires lors de la filamentation. Quant à l'application, il est important d'avoir une compréhension des mécanismes physiques présents lors de la filamentation induite par l'optique non linéaire. Étant donné de nombreux de phénomènes et d'applications de la filamentation, cette thèse se concentre sur une partie de ces aspects. Ceux-ci sont la rotation de la polarisation laser dans les gaz atomiques/moléculaires, le processus d'émission laser des molécules d'eau dans l'étalonnage air, lde l'humidité à travers la spectroscopie induite par un filament, ainsi que le renforcement de la fluorescence par un réseau de diffraction de plasma.

La rotation de la polarisation laser d'une sonde polarisée initialement linéaire a été étudié dans les gaz atomiques/moléculaires. Dans les gaz atomiques, la biréfringence ultrarapide induite par l'effet Kerr a été mesurée quantitativement. Dans les gaz moléculaires, la biréfringence et les états de polarisation de la production de la sonde ont été modulés à la renaissance rotationnelle de la molécule.

Également, nous avons étudié expérimentalement la fluorescence induite par filament à partir des fragments dissociés dans l'air. Les émissions de fluorescence des radicaux libres OH à 308.9 nm et NH à 336.0 nm ont été observés dans l'air. La fluorescence rétrodiffusée par le groupement OH et le groupement NH présentait une augmentation exponentielle accompagnant l'augmentation de la longueur du filament qui indique l'existence de l'émission spontanée amplifiée (ASE).

En plus, on étudie la spectroscopie de fluorescence induite par filament à partir du réseau de diffraction pour le plasma. Le réseau de diffraction pour le plasma a été généré par des filaments non colinéaires qui se superposés et synchronisés temporellement dans l'air. Une série de spectres des fragments excités du CN a été observée. L'intensité de fluorescence du radical CN en utilisant un réseau de diffraction

par le plasma est beaucoup plus forte que celle utilisant des filaments séparés temporellement.

Abstract

Femtosecond laser filamentation, which originates from a dynamic equilibrium between Kerr self-focusing and defocusing by the self-generated plasma produced by multiphoton/tunnel ionization of air molecules, has attracted a lot of scientific applications such as remote sensing of atmospheric pollutants, molecular identification by the alignment of molecules, etc. However, there are many nonlinear processes taking place during filamentation. From the application point of view, it is important to have a good understanding of the detailed physics behind filamentation induced nonlinear optics. Since there are many nonlinear phenomena and applications for filamentation, the thesis only focuses on few aspects of filamentation. Those are: the polarization rotation in atomic/molecular gases, the lasing action of water molecules in air, the humidity calibration through the filament-induced spectroscopy, as well as the fluorescence enhancement by plasma grating.

The polarization rotation of an initially linearly polarized probe pulse was studied in atomic/molecular gases. In atomic gases, the ultrafast birefringence induced by Kerr effect was quantitatively measured. In molecular gases, the birefringence and the polarization states of the output probe were modulated at the rotational revival of molecule.

We also experimentally investigate the filament-induced fluorescence from the dissociated fragments in air. Fluorescence emissions from OH free radicals at 308.9 nm and NH free radicals at 336.0 nm were observed in air. The backscattered fluorescence from both OH and NH exhibited an exponential increase with increasing filament length, indicating amplified spontaneous emission.

We have further investigated the filament-induced fluorescence spectroscopy from a plasma grating. The plasma grating was generated by non-collinearly overlapping temporally synchronized filaments in air. A series of spectral lines from the excited fragments of CN was observed. The fluorescence intensity from CN radicals in plasma grating was much stronger as compared to the case of temporally separated filaments.

Table of Contents

List of Tables

List of Figures

Acknowledgement

The work presented in this thesis is realized in the two ultra-short intense laser laboratories, one led by Prof. See Leang Chin in Laval University and the other by Prof. Heping Zeng in East China Normal University. First of all, I would like to thank my advisors, Prof. See Leang Chin and Prof. Heping Zeng for providing me with the great opportunity to join their groups and then bring me into the world of science. I am very grateful for their patience, support and guidance, and the opportunity they allowed me to direct the course of my research. Prof. Chin has taught me a lot of things whatever in research and in my life. Prof. Zeng is a very brilliant person and always provides me with resourceful ideas. After four years of study, I am feeling really "grown up" under their guidance.

Moreover, I would like to thank my colleague Prof. Tiejun Wang who helped me a lot in these four years. I can still remember that we worked together with great enthusiasm in our first project of THz generation. We have shared many things in these years and I have learned a lot from him. I also would like to express my deep gratitude to Dr. Feng Liang, Dr. Claude Marceau, Dr. Jean-Francois Daigle, Prof. Michel Piché, Prof. Bernd Witzel, Prof. Francis Théberge, Prof. Huailiang Xu, Prof. Yoshiaki Teranishi, Prof. Jian Wu, and Prof. Olga Kosareva for fruitful scientific discussions and Mr Mario Martin for his kindness and prompt technical assistances. I express my sincere gratitude to all the staff in COPL of Laval University and State Key Laboratory of Precision Spectroscopy of East China Normal University. I would also like to acknowledge those other people whom I have been fortunate to know and work with in the laboratory.

Finally, I acknowledge the Chinese Government Scholarships for Construction of High Level University graduate program as well as Prof. Chin and Prof. Zeng for the financial support.

Foreword

This thesis contains three published articles. I am the first author for each of them.

Chapter 3 Measurement of birefringence inside a filament. The results presented in this chapter are based on the following article: S. Yuan, T. J. Wang, O. Kosareva, N. Panov, V. Makarov, H. P. Zeng and S. L. Chin, "Measurement of birefringence inside a filament", Phys. Rev. A 84, 013838 (2011). It is the first paper during my doctorate study. I conducted experiments, analyzed the data and wrote the paper. But Prof. O. Kosareva did the simulations. Prof. Wang also helped me a lot during my experiment and Prof. Chin contributed the idea. Multiply revisions were done by Prof. Chin.

Chapter 5 Filament-induced lasing action. The results presented in this chapter are based on the following article. S. Yuan, T. J. Wang, Y. Teranishi, A. Sridharan, S. H. Lin, H. P. Zeng and S. L. Chin, "Lasing action in water vapor induced by ultrashort laser filamentation", Appl. Phys. Lett. 102 224102 (2013). I did the experiments, analyzed the data and wrote the paper. Prof. Chin contribute the idea. There were a lot of discussions between Prof. Wang, Prof. Teranishi, Prof. Chin and I.

Chapter 6 Humidity measurement using filament-induced fluorescence spectroscopy. The results presented in this chapter are based on the following article: S. Yuan, T. J. Wang, H. P. Zeng and S. L. Chin, "Humidity measurement in air using filament-induced NH fluorescence spectroscopy", Appl. Phys. Lett. 104 091113 (2014). In this work, I did most of the scientific work like contributing the idea, doing the experiment, analyzing the data and writing the paper. I also discussed a lot with Prof. Chin, Prof. Zeng and Prof. Wang.

Chapter 1 Introduction

1.1 Filamentation induced nonlinear optics

Femtosecond laser filamentation [1,2], which originates from a dynamic equilibrium between Kerr self-focusing and defocusing by the self-generated plasma produced by multiphoton/tunnel ionization of air molecules [1-6] has attracted much scientific interest. Great efforts by many groups have been made in order to understand the induced nonlinear optics.

In order to explain the filament formation, the self-trapping of a laser beam due to Kerr self-focusing was first proposed in 1964, by Chiao *et al.* [7]. Soon after that, many investigations on self-focusing in solids were conducted. In the 1970s, the filamentation phenomenon was observed by using nanosecond or picosecond pulses [8]. Of course, these research works were restricted by the laser technology at that time. Collisional processes take place when the pulse duration is longer than the electron collision time (~1 ps in atmospheric air or 1 fs in solids and liquids). They would strongly ionize the medium and mask the phenomenon of filamentation. With the evolution of laser technology, from the 1960s to the 1990s, the pulse duration has experienced significant reduction from nanosecond and picosecond to femtosecond. The development of the chirped pulse amplification (CPA) system (1985) [9], as well later the invention of the femtosecond Ti: Sapphire laser (1991) [10], offer opportunities for progress in ultrafast science. Nowadays, the output from a commercial femtosecond laser system has not only shortened the pulse duration, which prevents optical breakdown, but also maintains a strong peak intensity for filamentation.

When a high-power femtosecond laser pulse propagates in air, the intense light induced refractive index change will lead to self-focusing of the pulse. The filament is the result of a dynamic equilibrium between two nonlinear effects [11]: (a) Kerr self-focusing, resulting in an increase of the peak intensity of the pulse [1,3]; (b) plasma defocusing, which diffracts the pulse and decreases the intensity. The balance between these two processes clamps the pulse at a high intensity ~5×10^{13} W/cm^2 [1-5, 11,12] over a distance longer than the usual Rayleigh length. The result is a streak of weak plasma continuous spots. We call this a “filament”.

The first experimental result for filamentation in air was reported in 1995, by A. Braun *et al.* from Michigan University [13]. They found that after launching an intense near-infrared pulse in air, a self-induced plasma channel was generated, with a constant diameter of 100 μm. Soon after, research interest was focused on the physics and characterization of filamentation. In 2003, J. Kasparian et al, [14] produced a long white light laser filament in the atmosphere using a femtosecond-terawatt laser pulse in air. The backward scattered white light supercontinuum from the filament was observed along a distance of 10 kilometers.

Our group occupies a pioneering position in filamentation science. For example, we demonstrated the remote control of the onset of a filament by adjusting the initial diameter, the focal length of a lens/telescope and the pulse energy of the pulse [12,16]. More recently, Daigle *et al.* [17] successfully monitored the length and the ionization density of a filament by varying the diameter of an aperture in the laser beam path.

1.2 Potential applications

Nowadays, filamentation has become an essential issue in femtosecond laser science. Many nonlinear optical phenomena have been induced such as self-spatial filtering [18], intensity clamping [19], molecular alignment [20-22], supercontinuum generation [23], and so on, providing unique capabilities for applications like remote sensing [24-27], lightning control [28] or high harmonic [29], THz [30-34] and far-infrared pulse [35] generation. Here we just list some of the most important applications.

Terahertz pulse generation in filaments: Broadband THz pulses can be generated from filaments in a gas medium, through a process similar to Cherenkov radiation [36, 37]. THz radiation has potential applications in medical treatment, explosive detection, etc. However, since THz pulses are strongly absorbed by the water vapor in air, traditional THz sources from semiconductor antennae or nonlinear crystals cannot deliver THz radiation to long distances. A filament provides a new approach for generating THz radiation in air near a remote target [32,35-39]. Besides, since the emitter is a gas, it means there is no damage threshold limit at high intensities [35-40].

Filaments induced fluorescence spectroscopy (FIBS): The intensity inside the filament is about 5×10^{13}W/cm^2. Under this intensity, air molecules can be ionized, excited and emit fluorescence. The fluorescence spectroscopy from a filament indicates the components of the medium. Unlike the usual spectroscopic technique such as laser induced breakdown spectroscopy (LIBS) using nanosecond laser pulses, the FIBS is relatively “clean”, meaning that there is very little plasma continuum in the spectrum. This difference is attributed to the low density of the plasma inside the filament, which is between 10^{14} and 10^{16} cm^{-3} [1-5]. We name the FIBS as “fingerprint” spectroscopy [41, 42].

Molecular alignment induced by filamentation: The linearly polarized laser field inside a filament initiates an impulsive ‘kick’ to the air molecules. The molecules form an excited wave packet which is periodically aligned parallel to the laser’s linear polarization [43-50]. A molecule has its unique rotational states, meaning that one can identify the molecule by measuring the revival structure in the wake of a filament.

Filaments interaction: As two or more intense light filaments spatiotemporally overlap with one another, they experience robust interaction, which leads to many interesting phenomena like repulsion, fusion, and collision [51–56]. Strong coupling and fusion can be observed by overlapping two filaments. Especially inside the fusion region of two non-collinearly overlapped UV filaments, the peak electron density and the local field intensity are significantly enhanced [56].

1.3 Organization of this thesis

We have briefly talked about the historical background of filamentation and its applications. Nowadays, the understanding of the basic theory of filamentation has been well developed. However, the nonlinear optical phenomena induced by laser filamentation are still an ever-active subject, which leads to open questions and further applications. Besides, to show the detailed physical picture of the filament-induced nonlinear optical phenomena is not an easy subject, which requires decades of continuous scientific work. For instance, earlier publications have already investigated the birefringence inside a filament which results in the spatial separation of the laser beam pattern [68]. In their results, the birefringence was studied qualitatively, while it is still interesting for measuring the birefringence quantitatively, since the value of birefringence could help us identifying different gases. Aiming to investigate the nonlinear optical phenomena induced by filamentation in air, this thesis elucidates some characteristics of the nonlinear optics which are induced by laser filamentation.

In this thesis, we firstly quantitatively measure the birefringence in atomic/molecular gases (chapter 3 and chapter 4). The experimental results follow well our simulations. The evolution of the polarization states of an output probe polarization was elaborated as well. Afterwards, the lasing action in water vapor molecule and NH free radical inside a filament was demonstrated. The backscattered fluorescence from OH and NH radicals showed exponential increase with increasing filament length, indicating amplified spontaneous emission (chapter 5 and chapter 6). To our knowledge, it is the first time that lasing action is found in water vapor molecule and NH radical. The thesis is organised as follows:

Chapter two (filament-induced nonlinear optics and the laser chain): Chapter two provides a brief explanation of the filament-induced nonlinear optics. Filament-induced molecular alignment, polarization separator, lasing action and fluorescence spectroscopy are discussed. The laser chain which has been used for our present experimental work is also illustrated.

Chapter three (measurement of birefringence inside a filament in an atomic gas): Chapter three quantifies the ultrafast birefringence induced in the filament in an atomic gas by measuring the filament-induced polarization rotation of a probe pulse. In this chapter, an elaborate experimental study on nonlinear birefringence effects in filaments in argon is presented.

Chapter four (polarization evolution in the wake of molecular alignment inside a filament): In this chapter, we provide a detailed investigation on both major axis rotation and ellipticity evolution of a probe polarization ellipse at the molecular revival. The polarization rotation is due to the modulated birefringence by the alignment of molecular N_2.

Chapter five (lasing action induced by ultrashort laser filamentation): In this chapter, the water vapor fluorescence in air from filaments generated by intense ultrashort Ti:sapphire laser pulses is experimentally studied. By measuring the intensity inside the filament and the fluorescence intensity of OH, a high degree of nonlinearity is obtained, indicating a highly nonlinear field dissociation of H_2O molecule.

Chapter six (humidity measurement in air using filament-induced nitrogen monohydride fluorescence spectroscopy): In this chapter, strong fluorescence emissions from NH free radical at 336 nm were observed in air, when we applied water vapor to an intense femtosecond laser field. The generated NH radical is ascribed to chemical reaction between nitrogen and water vapor.

Chapter seven (identification of other molecules in air by using filament-induced fluorescence spectroscopy): A series of CN spectral lines are observed, as we detect the fluorescence from a filament by blowing CO_2 gas into the filament, which can be used to identify other molecules in air. We also propose a technique to enhance the fluorescence intensity by noncolinearly propagating two filaments in air.

Chapter eight (conclusion): Chapter eight reviews the contributions of this thesis.

Chapter 2 Filament-induced nonlinear optics

Self-guided propagation of ultrashort intense laser pulses in air was demonstrated to induce a filamentation channel [1-6]. Many interesting nonlinear optical phenomena inside the filament have been observed. The investigations on filament-induced nonlinear optics are a long term project, which is beyond the reach of my four years' doctorate. In this chapter, we give a brief explanation of the basic theory of filamentation and the mechanisms of some filament-induced nonlinear optics, which will be discussed later in this thesis. These nonlinear optical phenomena are: filament-induced polarization evolution in atomic gases (chapter 3); filament-induced molecular alignment and polarization separator in molecular gases (chapter 4); filament-induced lasing action (chapter 5) and filament-induced atmospheric sensing (chapter 6 and chapter 7).

2.1 Electromagnetic waves:

The propagation of an electromagnetic wave in a medium is governed by Maxwell's equations. In a nonmagnetic medium without free electron charges, Maxwell's equations are determined by [57,58]:

$$\nabla \cdot \vec{D} = 0, \tag{2.1.1}$$

$$\nabla \cdot \vec{B} = 0 \tag{2.1.2}$$

$$\nabla \times \vec{E} = -\frac{\partial \vec{B}}{\partial t}, \tag{2.1.3}$$

$$\nabla \times \vec{B} = \mu_0 \frac{\partial \vec{D}}{\partial t}, \tag{2.1.4}$$

where $\vec{E}$ is the electric field, $\vec{D}$ the electric flux density, $\vec{B}$ the magnetic induction, μ_0 the vacuum permeability. The relationship between the electric field $\vec{E}$ and the electric flux density $\vec{D}$ is given by $\vec{D} = \varepsilon_0 \vec{E} + \vec{P}$, where $\vec{P}$ is the polarization the medium, ε_0

the vacuum permittivity. Equivalently, we can expand the polarization $\vec{P}$ as a Taylor series [57,58]:

$$\vec{\mathrm{P}} = \chi^{(1)}\vec{E} + \chi^{(2)}\vec{E}^2 + \chi^{(3)}\vec{E}^3 + \chi^{(4)}\vec{E}^4 + \chi^{(5)}\vec{E}^5 ..., \tag{2.1.5}$$

where $\chi^{(2)}$, $\chi^{(3)}$ and $\chi^{(4)}$ are known as the second, third and fourth order tensors of nonlinear optical susceptibility, respectively. In isotropic materials e.g. in gases, due to the inversion symmetry, all even order terms on the right hand side of Eq. (2.1.5) must vanish, so

$$\vec{\mathrm{P}} = \chi^{(1)}\vec{E} + \chi^{(3)}\vec{E}^3 + \chi^{(5)}\vec{E}^5 ... \tag{2.1.6}$$

The electric field E is a time dependent function. By combining Maxwell's equations, the optical wave equation in nonlinear optics is obtained [57]:

$$\nabla \times \nabla \times \vec{E}(t) - \frac{1}{c^2}\frac{\partial^2 \vec{E}(t)}{\partial^2 t} = -\mu_0 \frac{\partial^2 \vec{P}(t)}{\partial^2 t}, \tag{2.1.7}$$

By omitting the high order terms of the susceptibility, the refractive index can be determined as a function of the intensity I of the field [57]:

$$\mathrm{n} = \mathrm{n}_0 + \mathrm{n}_2 I^2, \tag{2.1.8}$$

where the laser intensity I is:

$$I = \frac{n}{2n_0}|E|^2, \tag{2.1.9}$$

and the nonlinear refractive index

$$\mathrm{n}_2 = \frac{12\pi^2}{n_0^2 c}\chi^{(3)}. \tag{2.1.10}$$

n_2 is the Kerr term, which gives rise to the self-focusing which is essential for filamentation.

2.2 Self-focusing:

In Eq. (2.1.8), we can find that, as a high intensity laser pulse propagates in air, the refractive index not only depends on the linear refractive index of the medium, but also on intensity of the laser pulse. Considering a laser pulse with a Gaussian distribution of the pulse intensity in the beam cross section, due to the nonlinear Kerr effect (Eq. (2.1.8)), the central part of the pulse will see a higher refractive index than the outside part. As a result, when the pulse propagates, a phase difference between the central and the outside parts of the pulse is induced. As shown in Fig. 2.1, the refractive index difference will act as a positive lens, thus focusing the beam [1,12]. The critical power for self-focusing is [1,12]

$$P_c = 3.77\lambda^2 / 8\pi n_0 n_2, \tag{2.2.1}$$

For a near infrared pulse with 50 fs pulse duration, the critical power is measured to be about 10 GW in air [12].

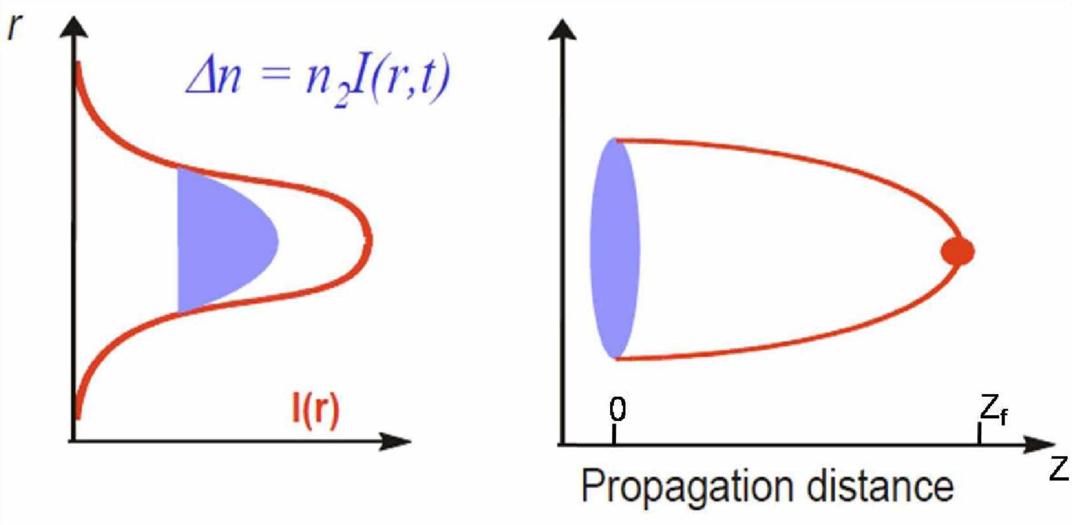

Fig. 2.1. The Kerr self-focusing effect. [1,59]

The self-focusing distance Z_f is given by Marburger's equation [1, 12]

$$Z_f = \frac{0.367 k a_0^2}{\left\{\left[\left(P/P_c\right)^{1/2} - 0.852\right]^2 - 0.0219\right\}^{1/2}}, \tag{2.2.2}$$

where k and a_0 are the wave number and the radius of the beam profile at $1/e^2$ level of intensity, respectively and P is the peak power of the pulse. In Eq. (2.2.2), once the peak power P increases, the self-focusing distance Z_f will decrease, meaning that the pulse focuses earlier. In case of external focusing, when the pulse is focused by an optical lens, the combined focusing distance Z_f' is given by the lens transformation formula [1,12,15]

$$Z_f' = \frac{Z_f f}{Z_f + f} \tag{2.2.3}$$

2.3 Intensity clamping:

For an intense fs laser pulse propagating in air with its peak power higher than the critical power for self-focusing, due to nonlinear Kerr effect, the pulse will self-focus in a slice-by-slice manner [6]. The local field intensity at the self-focus increases, resulting in the ionization of the air molecules. As a result, a weak plasma will be produced, which provides a negative change to the refractive index, hence defocusing the pulse [Fig. 2.2]

$$\Delta n_{plasma} = -\frac{e^2 N_e(t)}{2m_e \varepsilon_0 \omega_0^2}, \tag{2.3.1}$$

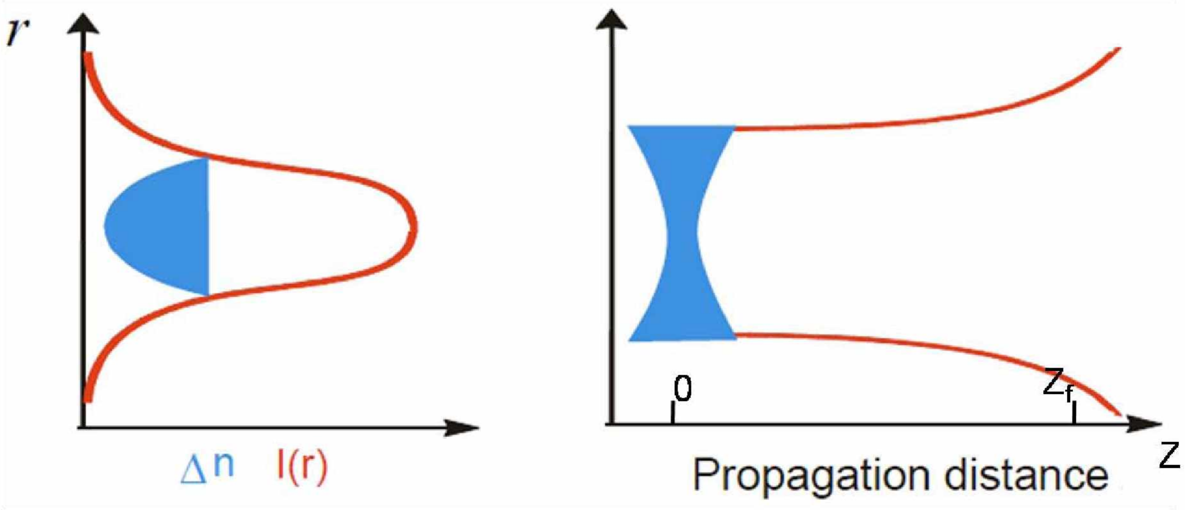

Fig. 2.2 The plasma induced defocusing of the pulse. [1,59]

where $N_e(t)$ is defined as the time dependent electron density, e and m_e are the electronic charge and mass, respectively, and ω_0 the central frequency of the laser pulse. At the beginning, the new generated plasma is rather weak. The pulse keeps focusing, as long as $n_2 I > \frac{e^2 N_e(t)}{2m_e \varepsilon_0 \omega_0^2}$. The ionization mechanism is effectively tunneling ionization. For the ease of our discussion without loss of generality, $N_e(t)$ is generated through a high order process; hence proportional to I^m, where m is not an integer, m measured to be around 11 for N_2 and 8 for O_2 [60,61]. By applying a proportionality constant k, the effective nonlinear refractive index change is given as a function of the field intensity, which is

$$\Delta n_{effective}(I) = n_2 I - \frac{e^2 N_e(t)}{2m_e \varepsilon_0 \omega_0^2}, \tag{2.3.2}$$

In Eq. (2.3.2), since the second term at the right-hand side (plasma term) is a high order term, as the intensity increases, it will soon catch up with the first term. In the end, when the two terms are equal, equilibrium between the self-focusing and the plasma induced defocusing takes place. The intensity could not increase further and is clamped, at a value which is ~5×10^{13} W/cm^2 in air [1, 62, 63].

2.4 Filament induced alignment of the molecules

One of the many important potential applications of filamentation is molecular alignment.

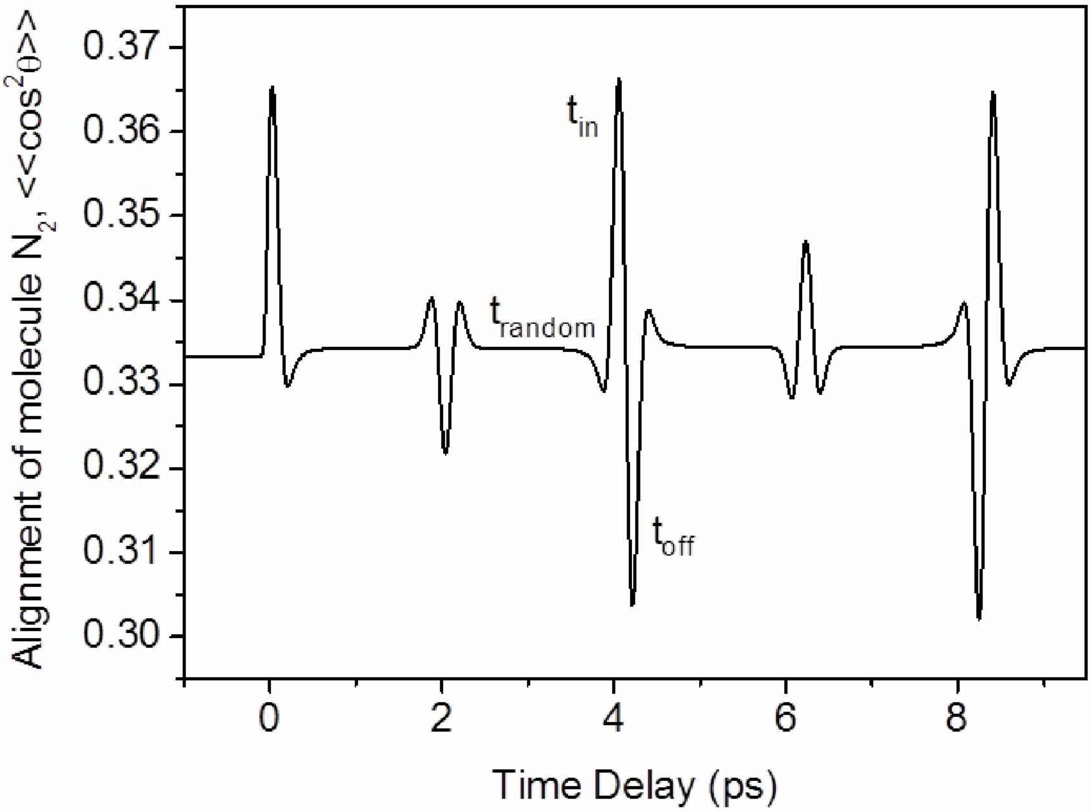

Fig. 2.3 The theoretical calculation of the alignment of N_2 molecules in air (from the author).

Different from ns pulse induced molecular alignment, which is an adiabatic process, inside the laser filamentation, the electric field gives an instantaneous quantum "kick" to the molecules, which creates the excitation of different rotational Raman states (nonadiabatic process). When the pulse passes, because the excited state life time is of the order of nanoseconds (ns), various rotational wave packets still exist, which exhibit "interference" structure at various revival times. The molecular alignment degree is averaged over all thermally populated rotational states of the involved molecules, yielding a statistic metric $\ll\cos^2\theta\gg$, which is a complex function of the ambient temperature T, the spatiotemporal characteristics of the exciting field $E(x,y,t)$, and the molecular polarizability anisotropy [64] [see Fig. 2.3]. In Fig. 2.3, T_{in}, T_{off}, and T_{random}

are defined as the in phase alignment, off phase alignment, and random distribution of molecules, respectively.

The molecular alignment will modulate the third order susceptibility in the wake of a filament, with the modulation depth depending on the pulse duration and the peak intensity of the pulse. The index of the refraction change in the direction of the pump polarization is

$$\delta n_{mol}(r,t) = 0.5(N_0\Delta\alpha / n_0)(\langle\langle\cos^2\theta(t)\rangle\rangle - 1/3) \tag{2.4.1}$$

where N_0 is the molecular density, $\Delta\alpha$ the effective polarizability of the medium, n_0 the linear refractive index, and $(\ll \cos^2\theta(t) \gg -1/3)$ denotes the direction of the molecular axis [45].

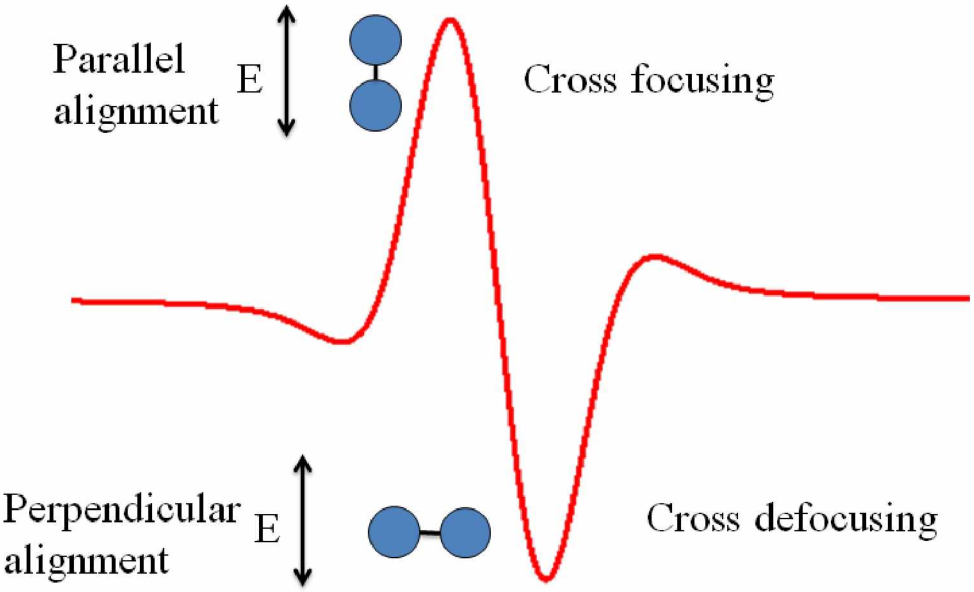

Fig. 2.4 Cross focusing and defocusing at molecular revival

In the wake of the filamentation, the molecules in air are aligned periodically, with in phase and out-of-phase revivals [see Fig. 2.3]. We consider a pump-probe experiment in air. The pump and probe pulses have the same initial polarization. The pump pulse creates a filament, while the weak probe pulse detects (probes) the change in index of refraction of the filament zone as the delay time between the pump and the probe changes. At the in-phase revivals $(\ll \cos^2\theta(t) \gg -1/3) > 0)$, the molecular axis are aligned along the pump polarization direction. Due to $\delta n_{mol}(r) > 0$ and $\delta n_{mol}(r) \sim I(r)$, the alignment induced refractive index change will act as a positive lens for the probe pulse, which strengthens the focusing process of the probe [see the parallel alignment in Fig. 2.4]. While at the out-of-phase revivals ($\ll \cos^2\theta(t) \gg -1/3) < 0$, the molecules are aligned perpendicular to the pump polarization direction. Due to $\delta n_{mol}(r) < 0$ and $\delta n_{mol}(r) \sim I(r)$, the refraction will defocus the probe [see the perpendicular alignment in Fig. 2.4].

2.5 Filament induced polarization separator

A high intensity laser filament will change the birefringence in a gas medium. In atomic gases, an instantaneous birefringence is created by the electronic cross-phase modulation (XPM). In molecular gases, besides this instantaneous electronic response, a delayed birefringence effect is induced by the impulsive molecular alignment with periodic revivals after the excitation of the filament [44-50]. The birefringence turns the filament into a polarization separator.

If we consider another pump-probe experiment in a gas medium, the high intense pump pulse creates the filament, while the probe pulse propagates collinearly with the pump. In atomic gases, when the pump and the probe pulses overlap, an instantaneous electronic XPM will take place. It results in a refractive index difference Δn_{probe} between the parallel and orthogonal components of the probe according to the pump polarization direction, by considering $\chi^{(3)}_{xxxx} = 3\chi^{(3)}_{yyxx}$ [57]. Thus, $\Delta n_{probe} = \Delta n^{XPM}_{probe}$. In molecular gases (We did not take into account the electronic XPM effect at initial revival), the refractive index modulation along (δn^{align}_X) and perpendicular (δn^{align}_Y) to the laser field is given by [9,14]

$$\delta n^{align}_X(r,t) = \frac{2\pi N}{n_0}\Delta\alpha(<< \cos^2\theta >>_t -1/3) \tag{2.5.1}$$

$$\delta n^{align}_Y(r,t) = -\frac{\pi N}{n_0}\Delta\alpha(<< \cos^2\theta >>_t -1/3) \tag{2.5.2}$$

where N and n_0 are the molecular number density and linear refractive index of the initially randomly aligned molecules respectively, $\Delta\alpha$ the molecular polarizability anisotropy and $(\ll \cos^2\theta(t) \gg -1/3)$ denotes the direction of the molecular axis. Since the plasma defocusing has no preference along or perpendicular to the laser polarization, the resulting birefringence $\Delta n_{probe}(r,t)$ in alignment revival is derived as

$$\begin{aligned}\Delta n^{align}(r,t) &= \Delta n_{probe}(r,t)\\ &= (\delta n_X^{align}(r,t) + \Delta n_{plasma}(r,t)) - (\delta n_Y^{align}(r,t) + \Delta n_{plasma}(r,t))\\ &= \delta n_X^{align}(r,t) - \delta n_Y^{align}(r,t) = \frac{3\pi N}{n_0}\Delta\alpha(<<\cos^2\theta>>_t - 1/3)\end{aligned} \tag{2.5.3}$$

Δn_{probe} takes different forms in atomic gases

$$\Delta n_{probe} = \Delta n_{probe}^{XPM} \tag{2.5.4}$$

and in molecular gases at revival

$$\Delta n_{probe}(r,t) = \frac{3\pi N}{n_0}\Delta\alpha(<<\cos^2\theta>>_t - 1/3), \tag{2.5.5}$$

The birefringence induces dephasing between the probe beam components along and perpendicular to the pump polarization direction [65-67]

$$\varepsilon = 2\pi\int \Delta n_{probe} dz / \lambda_{probe} \quad . \tag{2.5.6}$$

Through propagation, the probe nonlinear phases along and perpendicular to the pump laser field are accumulated separately over the filament length. The dephasing ε at the output would give rise to a polarization rotation of the output probe and convert the initial linear polarization of the probe into elliptical [66-68]. The polarization rotation angle φ, which is defined as the angle of rotation of the major axis of the elliptically polarized probe after propagating through the filament with respect to its initial polarization direction [see Fig. 2.5], can be retrieved through applying the dephasing ε into

$$\cos\varepsilon = \frac{E_x^2 - E_y^2}{2E_xE_y}\tan 2(\psi_{probe} + \varphi)\,, \qquad (2.5.7)$$

where ψ_{probe} is the initial angle between the linear probe polarization and the x axis.

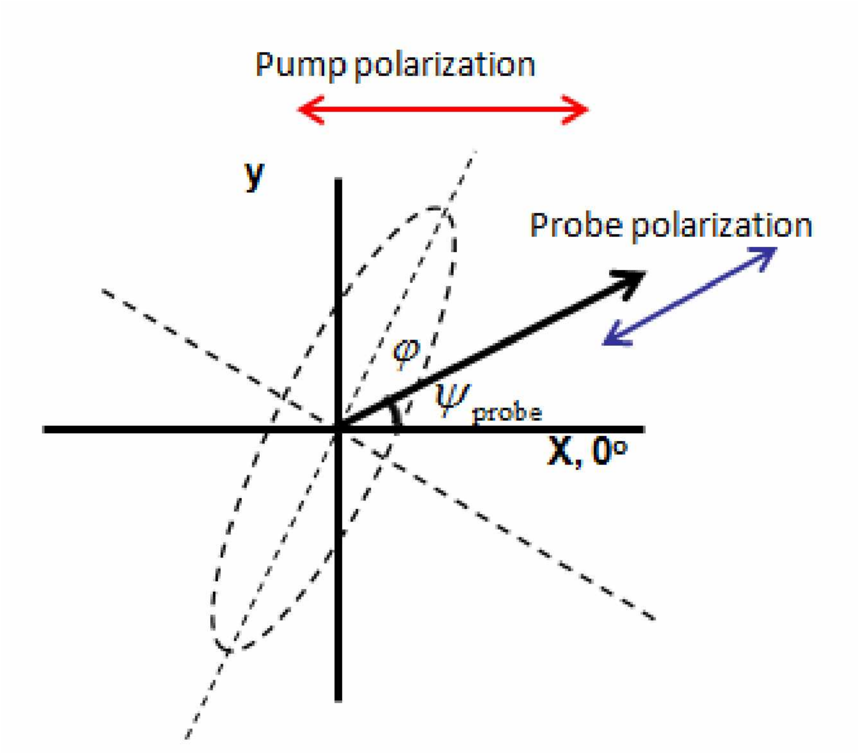

Fig. 2.5 The polarization scheme for the probe.

By using the polarization separator effect in filament, the polarization of a probe pulse can be easily manipulated by changing the polarization of the pump or even by simply tuning the relative delay between the pump and the probe in molecular gases.

2.6 Filament induced lasing action

The high intensity inside a laser filament not only ionizes air molecules but also excites the molecules and ions into highly excited states emitting “finger print” fluorescence [41, 42]. Sometimes, the fluorescence intensity of the ions/atoms/molecules in backward or forward direction of the filament shows an exponential increase with increasing filament length. This is called amplified spontaneous emission (ASE) lasing. The ASE lasing has been reported in a lot of ions or dissociated fragments from filamentation, e.g. N_2 and N_2^+ in air [11,69-81], OH [82] and NH [83] by heating a water bath beneath the filament in air, CN in ethanol flame [84], CH in air hydrocarbons gas mixture [85].

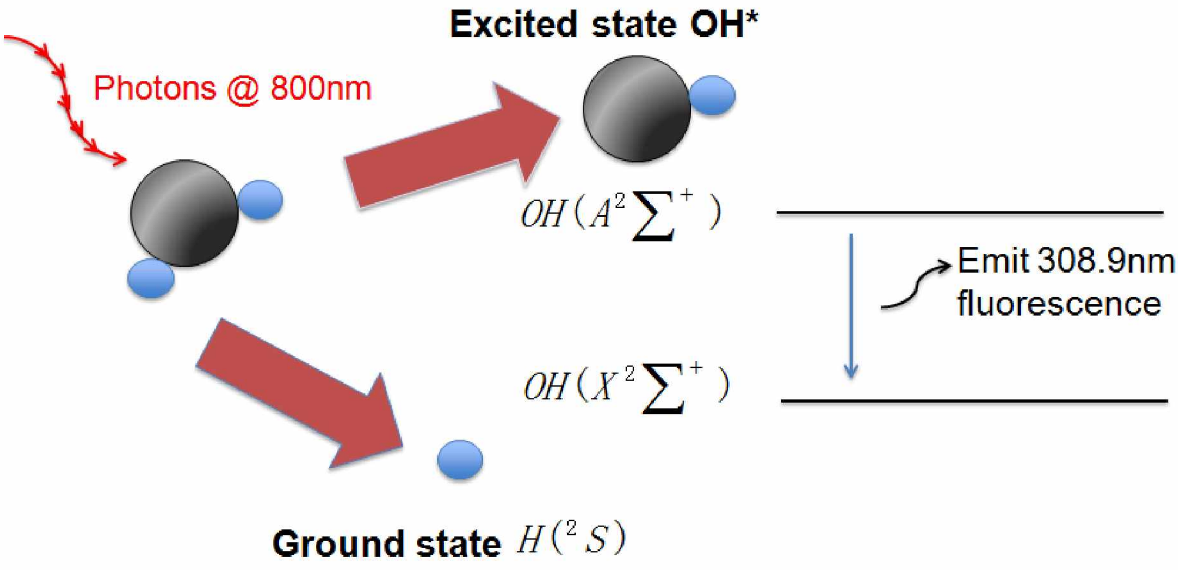

Fig. 2.6 Multi-photon dissociation of the H_2O molecule in air and subsequent excitation of the OH fragment result in emission at 308.9 nm.

An ultrafast laser filamentation can easily dissociate the gas medium, resulting in two or more fragments. In a high intensity laser field, a number of high lying channels yielding some fragments in the excited states are observed. For instance, in Fig. 2.6, the water vapor molecules are dissociated, through $H_2O + nh\nu \rightarrow H(^2S) + OH(A^2\Sigma^+)$. The fragment OH in the excited state OH(A) is generated. On the other hand, the ground states of fragment OH(X) is initially empty. Thus the population is naturally inverted, and ASE lasing occurs.

2.7 Filamentation for atmospheric sensing

Self-guided propagation of femtosecond laser filamention clamps a high intensity ($\sim 5\times10^{13}$ W/cm^2 [1-5]) over a long distance. Under this intensity, air molecules are excited, which induces some "finger print" fluorescence [41,42]. By using this fluorescence technique, other molecules in the atmosphere can be detected.

In recent years, nanosecond laser-induced breakdown spectroscopy (LIBS) has become a powerful technique for atmospheric measurements and detection of biological agents [86,87]. However, in nanosecond timescale, too much energy is absorbed from the laser radiation through inverse Bremsstrahlung and cascade ionization [88]. In this case, the molecules might be totally dissociated into atoms. Thus, from the LIBS, it is rather difficult to see the transition between molecular states. However, in the filament-induced spectroscopy, since the fs-pulse-induced free electrons do not have enough time to absorb too much energy, the plasma density (10^{14}–10^{16} cm^{-9}) and temperature (5800 K) are relatively low [1,42,89,90]. Therefore, the detailed molecular states can be detected by this spectroscopy and the filament-induced spectra are free from the plasma effect, thus very “clean” [see Fig. 2.7].

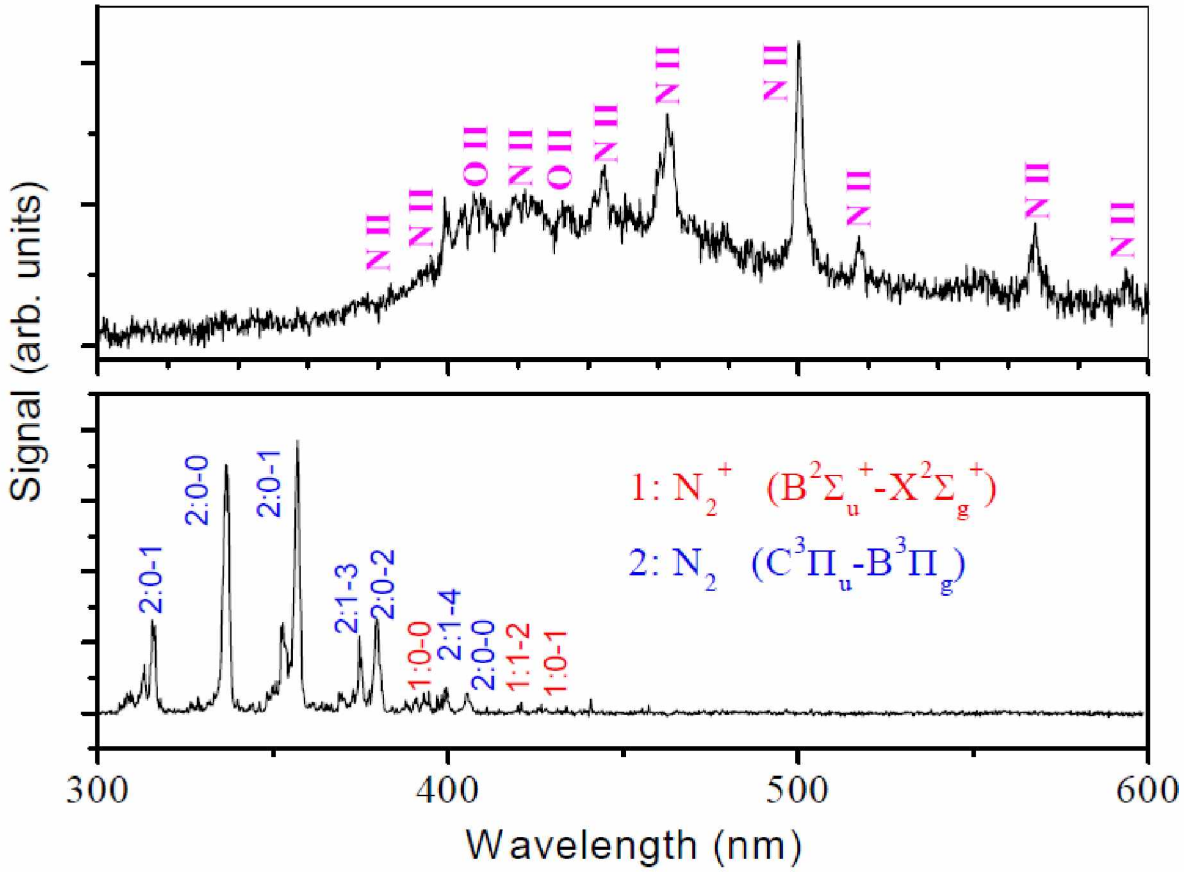

Fig. 2.7 Long pulse-induced breakdown and short pulse filament-induced fluorescence spectra of air obtained in the ambient atmosphere. For both cases, the energy per pulse was 5 mJ. The durations of the short and long laser pulses were 42 fs and 200 ps, respectively [42,95]

In addition, the filament self-transforms into white-light pulse with an extraordinary broad spectral content ranging from IR to UV [91-93]. The backscattered white light fluorescence can be detected over a distance of 20 km [14]. Therefore, one can expect to detect pollutant molecules in the atmosphere even remotely. In 2008, experimental results have shown filament-induced spectra from burning mosquito coils in air, with spectral lines from molecular fragments like CN, CH and C_2 [94]. Moreover, the spectra from the mixture of hydrocarbon gases ($CH_4/C_2H_2/C_2H_4$) and air were measured at a distance of 118 m from the laser source, through LIDAR detection technique. Distinctive CH band was found between 428-431nm [27].

2.8 Laser chain

The laser chain which has been used for the experiments in this thesis is schematically shown in Fig. 2.8.

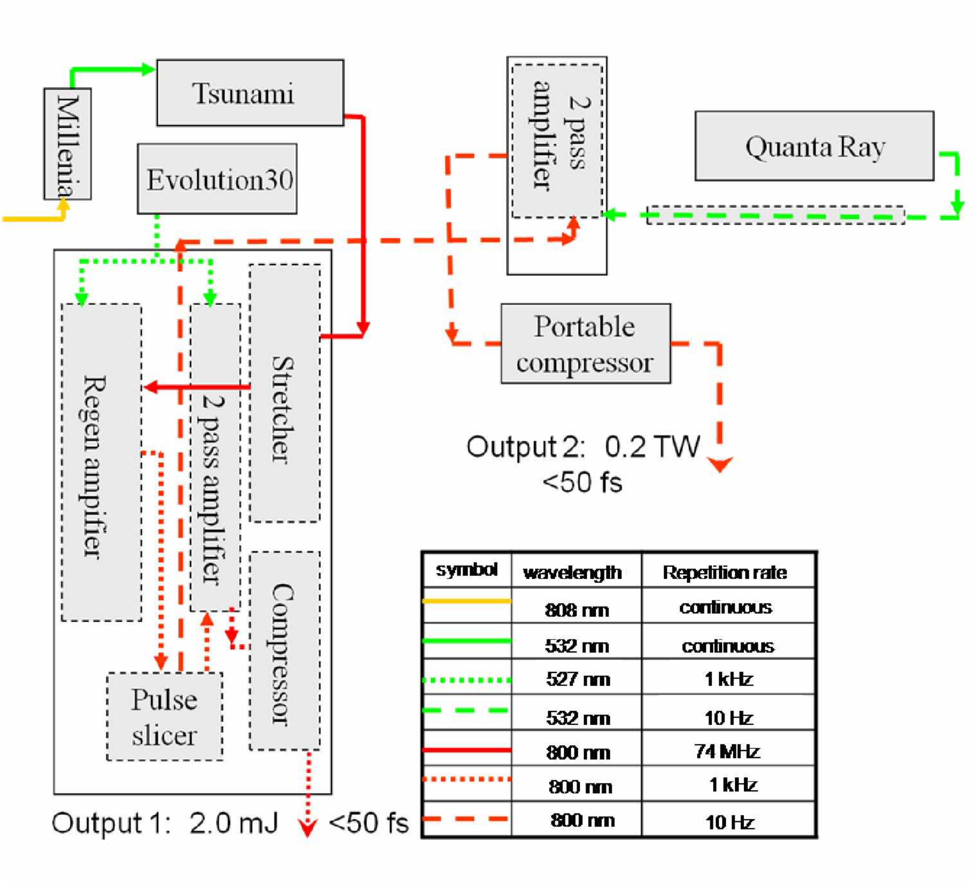

Fig. 2.8 The laser system used for this thesis [96]

A diode pumped solid-state laser system (Millenia) works as a pump for the mode-locked Ti:Sapphire oscillator. The seed from the oscillator is sent into the chirped pulse amplification (CPA) system (Spitfire, Spectra Physics) with a stretcher, a regenerative amplifier, a 2 pass amplifier and a compressor.

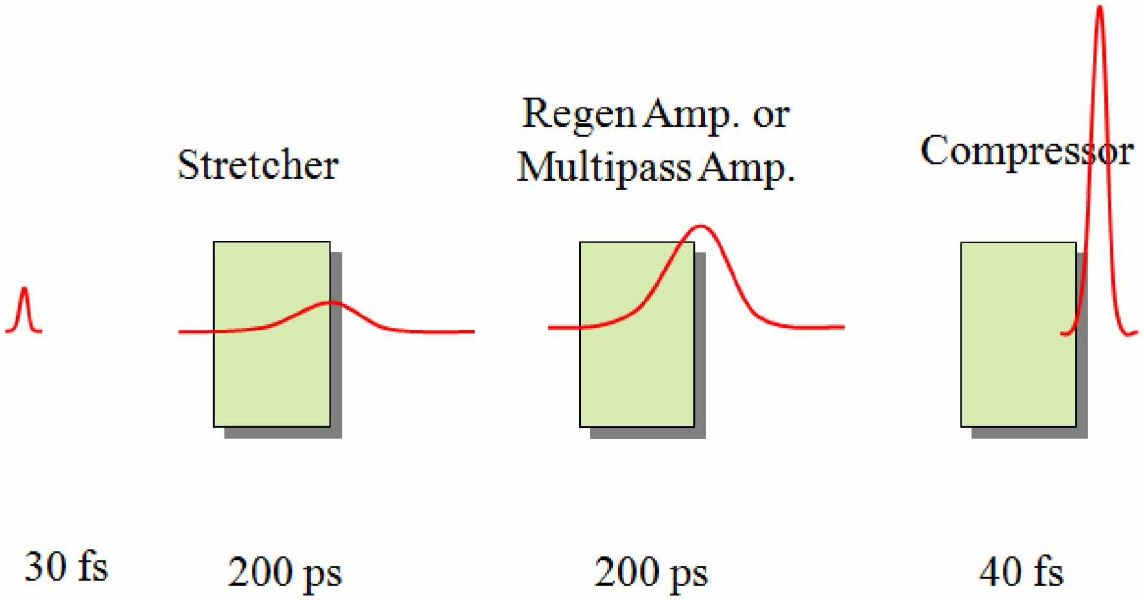

Fig. 2.9 Scheme for CPA technique

In the CPA chamber [see Fig. 2.9], the seed beam is stretched to around 200 ps in the stretcher and then directed to the regenerative amplifier in order to prevent self-focusing effect caused by high intensity. The regenerative amplifier was pumped by a green laser beam at 527 nm. The stretched seed pulse was amplified in the regenerative amplifier over several round trips. The amplified pulse is switched out at the right moment with enough energy and it is then sent to another two-pass amplifier. After the 2-pass amplifier, the laser pulse is compressed by the compressor and finally gives 2 mJ for the pulse energy, 50 fs for the pulse duration at FWHM with repetition rate of 1 kHz as the output (output-1). Most of the experiments in this thesis were done by using this output.

The pulse slicer [see Fig. 2.8] separates a 10 Hz beam from the output of the regenerative amplifier as the seed of output-2. This pulse is delivered to another two-pass amplifier, which is pumped by the 500 mJ/pulse with repetition rate of 10 Hz from a commercial Nd:YAG laser system (Quanta-Ray from Spectra Physics). After that the laser pulse is sent to a portable compressor to achieve 13 mJ for the pulse energy and 50 fs for the pulse duration at FWHM in the end (output-2). One measurement in Chapter 5 in this thesis has employed this output. The inset table shows the characteristic of the beam propagating in the laser chain.

Chapter 3 Measurement of birefringence inside a filament[1]

3.1 Introduction

Intense femtosecond laser pulse propagation in air shows a unique property which is called filamentation. Filamentation in air results from a dynamic interplay between self-focusing induced by the neutral air molecules and defocusing from the plasma produced via multiphoton/tunnel ionization of air molecules [1-6], providing unique capabilities for applications like remote sensing [41,42], lightning control [28] or high harmonic [29], THz [30-34] and far-infrared pulse [35] generation.

A high-intensity laser field will induce birefringence in the initially isotropic optical medium which can change the polarization of a probe pulse. The linearly polarized probe pulse becomes elliptically polarized whose major axis rotates in the course of propagation [98]. Recently, it was proved by Béjot *et al.* [99] thatfilament -induced symmetry breaking in argon gas can act as a "gaseous half wave-plate" for the probe. Later Marceau *et al.* [68], Chen *et al.* [100] and Calegari *et al.* [101] demonstrated that filament in molecular gases can spatially separate the orthogonal polarizations of a probe pulse with the parallel-to-pump polarization component guided along the propagation axis, and the perpendicular-to-pump polarization component defocused outside. More recently, based on the vectorial model [102], the key role of the probe pulse cross-focusing was shown to be the reason for the polarization ellipse rotation.

In this chapter, we provide a new technique to quantify ultrafast birefringence by measuring the rotation angle of the major axis of the probe elliptical polarization induced by cross-phase modulation (XPM). Since no special time-resolved detection is required, this simple technique can in principle be applied to any wavelength in transparent atomic gases and could even be extended to molecular gases. Unlike previous ultrafast birefringence measurements done by measuring the spectral modulation [65], or through a time domain treatment of pump-probe experiments

---

[1] The results presented in this chapter are based on the following article. S. Yuan, T. J. Wang, O. Kosareva, N. Panov, V. Makarov, H. P. Zeng and S. L. Chin, "Measurement of birefringence inside a filament", Phys. Rev. A 84, 013838 (2011).

[103,104], by using this technique, we can directly give the probe elliptical polarization states after the filament. In terms of understanding the physics, we demonstrate that the filament-induced polarization rotation angle of the probe is related to the ellipticity of the probe polarization. That means at a certain probe polarization rotation angle, it will have a fixed ellipticity of the probe polarization. This could happen both after and within the filament region. It might benefit to verify the polarization states of the probe from their experimental results or theoretical calculations.

3.2 Experiment setup

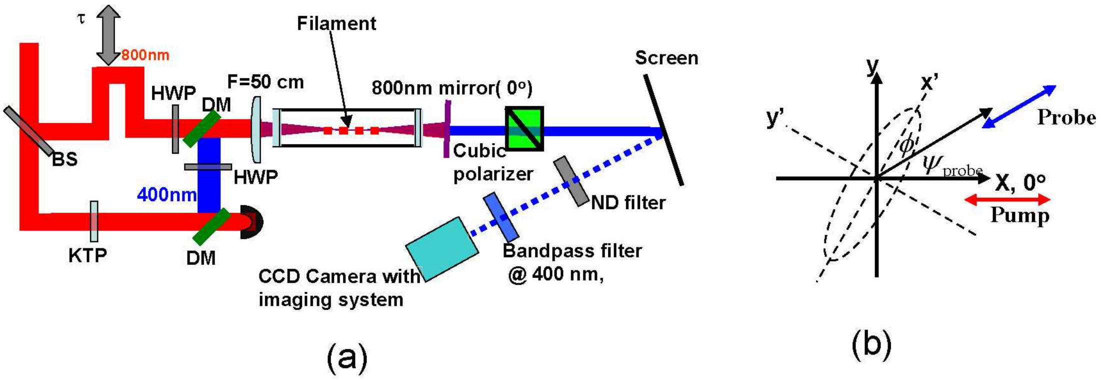

Fig. 3.1 (a) Schematic diagram of our experimental setup. Time delay of the pump pulse (800 nm) can be changed by a delay line. DM: dichroic mirror; BS: beam splitter; HWP: half-wave plate; CCD: charge coupled device. (b) The polarization scheme for the probe.

Our experimental setup is shown in Fig. 3.1. The output of a Ti:sapphire laser (10 Hz, 50 fs, 800 nm) was split into two parts by a beam splitter (BS) with 70% reflection and 30% transmission. The reflected pulse with 1.1 mJ was used as the pump and generated a 2 cm-long filament at the center of an 80-cm-long gas cell filled with argon (purity>98%) at one atmospheric pressure. Here the critical power for self-focusing is estimated to be 10 GW [12], corresponding to 0.5 mJ for pulse energy in our laser output. The experiment was operated in a stable and single filament condition. The transmitted beam passed through a 100-μm-thick KTP crystal for second harmonic generation and was reflected by two dichroic mirrors (DM, with a high reflectivity of 99.5% at 400 nm and high transmission of 90% at 800 nm) to filter out the remaining 800 nm. The resulting pulse was set as probe (2.7 μJ, less than 100 fs, 400 nm). The pump and probe beams were combined together by the second DM. Two half-wave plates (HWP) for 800 and 400 nm were mounted on the pump and probe beam paths, respectively. Both beams were initially prepared in parallel linear polarizations, and focused by a plano-convex lens with a focal length of 50 cm. During the experiment, the angle between the polarizations of the pump and probe was varied according to the experimental design (see below). After the filament, a dichroic mirror was used to block the pump beam while transmitting the probe. A white paper screen was set around 1 meter after the filament. A CCD camera covered by several neutral density (ND) filters and a band-pass filter centered at 400 nm (bandwidth = 80 nm) was used to image the transmitted probe pattern on the screen so as to record the fluence distribution of the probe scattered on the screen. A CCD camera was used in this experiment instead of a photodiode since it could benefit us for better understanding the guiding and diffraction effect inside the filament by detecting the spatial distribution of the probe. In our experiment the transverse size of the probe beam, in which the polarization is essentially rotated, is similar to that of the filament, since the probe has the same initial diameter as the pump, is focused by the same lens, and experiences nonlinear cross focusing induced by the pump. The bandwidth of the filter was large enough to cover the full spectral width of the probe, including its spectral broadening due to XPM in the filament [65]. The polarization of the probe beam was analyzed by a cube polarizer after the dichroic mirror. In order to adjust the relative delay between the pump and probe pulses, we installed a motorized translation stage on the pump beam path. This experiment was done with a good temporal overlap for the pump and probe, as described in ref. [65]. We note that the probe pulse probed the filament core of the pump because they were both focused by the same lens and because the filament would guide the probe pulse [100,102]. Also during the experiment, we did not observe any white light from our optics. This indicates that the effect of the optical components was minimized to the extent that it did not affect our results significantly, unlike the case of the self-compressed pulse propagation through glass [105].

3.3 Theoretical analyses

The mechanism of the measurement technique can be explained by the difference in the non-linear refractive indices generated by the driving laser field along its polarization axis (parallel or x-axis, see Fig. 3.1b) and the orthogonal y-axis. Integrated over the whole interaction length, the birefringence induces a dephasing between the probe beam components along the fast and slow polarization axes [99]

$$\varepsilon = 2\pi \int \Delta n_{probe}^{XPM} dz / \lambda_{probe} \quad , \tag{3.3.1}$$

where Δn_{probe}^{XPM} is the XPM-induced index change between the parallel and orthogonal components of the probe by considering $\chi_{xxxx}^{(3)} = 3\chi_{yyxx}^{(3)}$ [98], and λ_{probe} is the wavelength of the probe pulse. The birefringence is quantitatively characterized by the dephasing ε (phase difference between the parallel and orthogonal components of the probe pulse), which is related to the XPM-induced refractive index change, the pump and probe interaction length and the filament intensity.

We choose a laboratory coordinate system shown in Fig. 3.1(b) to describe the two components of the probe field along the fast (orthogonal, y) and slow (parallel, x) polarization axes:

$$E'_{2\omega x} = E_{2\omega x}\cos(\omega t - kz), \tag{3.3.2}$$

$$E'_{2\omega y} = E_{2\omega y}\cos(\omega t - kz + \varepsilon), \tag{3.3.3}$$

where $E_{2\omega x}$ and $E_{2\omega y}$ are the electric fields of the probe pulse projected on the fast (y) and slow (x) polarization axes before interacting with the pump while $E'_{2\omega x}$ and $E'_{2\omega y}$ are the ones after interaction with the pump inside the filament. By doing coordinate rotation from the laboratory coordinate system (x,y) to the probe coordinate system (x',y'), where x' is parallel to the major axis of the rotated probe ellipse, we obtain [67]:

$$\cos\varepsilon = \frac{E_{2\omega x}^2 - E_{2\omega y}^2}{2E_{2\omega x}E_{2\omega y}}\tan 2(\psi_{probe} + \phi), \tag{3.3.4}$$

$$e^2 = \frac{(\frac{E_{2\omega y}}{E_{2\omega x}})^2 + \tan^2(\psi_{probe} + \phi) - 2(\frac{E_{2\omega y}}{E_{2\omega x}})\tan(\psi_{probe} + \phi)\cos\varepsilon}{(\frac{E_{2\omega y}}{E_{2\omega x}})^2\tan^2(\psi_{probe} + \phi) + 1 + 2(\frac{E_{2\omega y}}{E_{2\omega x}})\tan(\psi_{probe} + \phi)\cos\varepsilon}, \tag{3.3.5}$$

where ψ_{probe} is defined as the initial angle between the linear probe polarization and the x axis [Fig. 3.1(b)] and ϕ as the angle of rotation of the major axis of the elliptically polarized probe after propagating through the filament with respect to its initial polarization direction. With Eq. (3.3.4), the dephasing ε can be obtained from the measured rotation angle ϕ while using Eq. (3.3.5). the ellipticity e of the probe polarization, defined as $e = \frac{E'_{2\omega y}}{E'_{2\omega x}}$, can be evaluated by using the dephasing ε and the rotation angle ϕ.

3.4 Experimental results and discussions

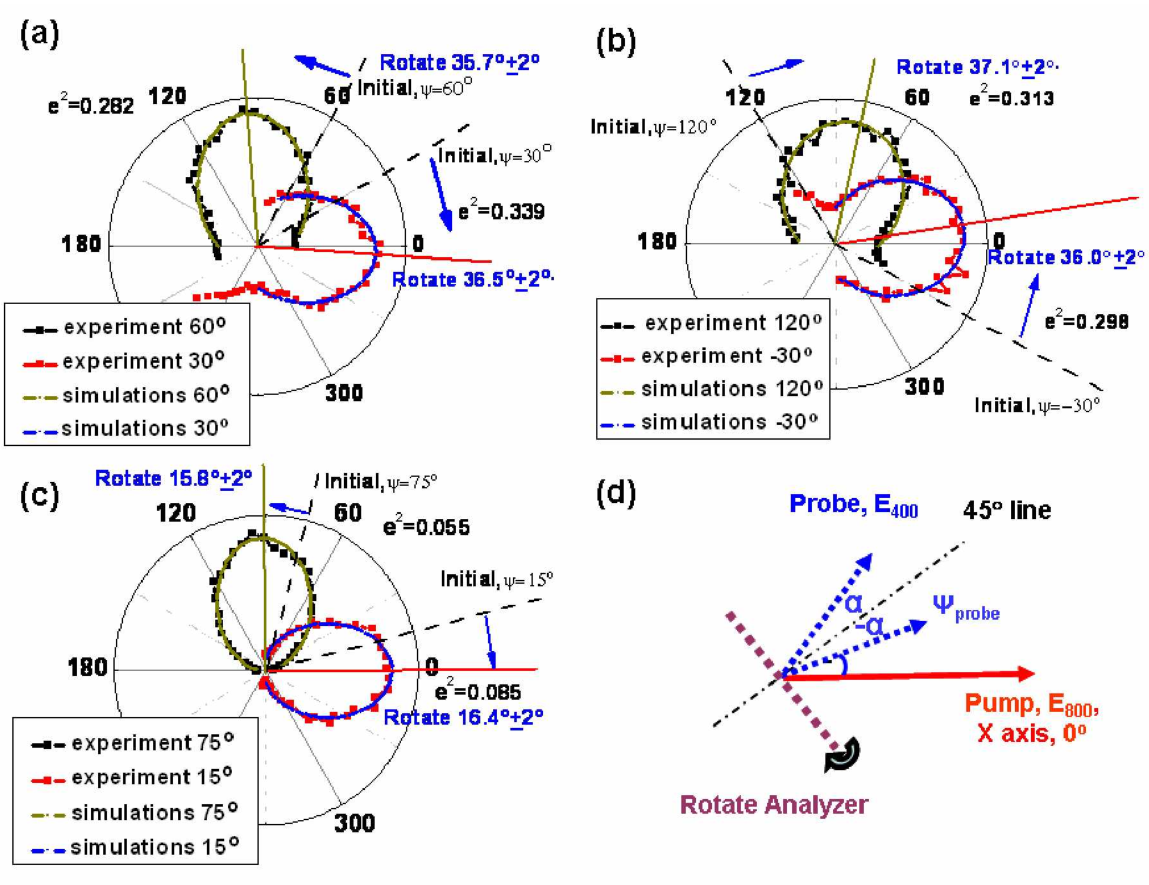

Fig. 3.2 Polarization analysis of the transmitted probe at the end of filament for pairs of initial probe polarization angles ψ_{probe} at 60° and 30° (a), 120° and -30° (b), 75° and 15° (c), with polarization scheme of the pump, probe and analyzer (d). Dash straight lines and solid straight lines correspond to probe polarization after the analyzer when the pump is turned off (initial) and on (final), respectively. XPM induced polarization rotations are marked by the blue arrows and characters. The simulations are Lorentz fitting of the experimental curves.

The experiment was carried out by rotating the transmission axis of the analyzer with the pump and probe initial linear polarization directions fixed. The probe polarization transformation after passing through the filament was studied for various pairs of the initial probe polarization angles +α and -α, symmetric relative to the 45° line (with respect to the x-axis) in Fig. 3.2(d). The x-axis (0°) in this experiment was defined parallel to the fixed pump polarization [see Fig. 3.2(d)]. The polarization states of the probe accumulated along the filament were measured by rotating the analyzer transmission axis. These states are shown in Figs. 3.2(a, b, c), which respectively correspond to the initial probe polarization angles ψ_{probe} = 45° ± 15° = 60° and 30°, ψ_{probe} = 45° ± 75° = 120° and -30° and ψ_{probe} = 45° ± 30° = 75° and 15° respectively. After propagating through the filament, the probe polarization integrated over the whole beam became elliptical, with the major axes rotated.

Initial Probe polarization (ψ_{probe})	Experimental probe rotation angle (major axis)	Dephasing (ε)	Calculated ellipticity square ($e^2_{simulation}$)	Experimental ellipticity square ($e^2_{\exp eriment}$)
15°	$16.4^{\circ}\pm2^{\circ}$	$(0.527\pm0.030)\pi$	0.075	0.085
30°	$36.5^{\circ}\pm2^{\circ}$	$(0.537\pm0.025)\pi$	0.321	0.339
60°	$35.7^{\circ}\pm2^{\circ}$	$(0.542\pm0.014)\pi$	0.329	0.282
75°	$15.8^{\circ}\pm2^{\circ}$	$(0.515\pm0.039)\pi$	0.071	0.055
-30°	$36.0^{\circ}\pm2^{\circ}$	$(0.539\pm0.011)\pi$	0.328	0.298
120°	$37.1^{\circ}\pm2^{\circ}$	$(0.547\pm0.029)\pi$	0.325	0.313

Table 3.1. Measured the probe major axis rotation angle, the dephasing coefficient (ε), and the ellipticity square for the probe polarization theoretically ($e^2_{simulation}$) and experimentally ($e^2_{\exp eriment}$).

Table 3.1 summarizes the experimentally measured rotation angles and dephasing ε of different initial probe polarizations, and the corresponding calculated and measured ellipticities squared. The measured ellipticity is defined as the ratio between the length of the minor axis and that of the major axis on the Lorentz fit (solid curves in Fig. 3.2a-c) onto the experimentally measured angular transmission (squares in Fig. 3.2a-c). The calculated ellipticity square ($e^2_{simulation}$) is derived from Eq. (3.3.5). The dephasing ε is obtained using Eq. (3.3.4) together with the measured probe polarization rotation angle. The calculated ellipticities ($e^2_{simulation}$) are in good agreement with the directly measured ones ($e^2_{\exp eriment}$). This not only convincingly verifies the accuracy of the technique, but also indicates an underlying physical connection between the probe polarization rotation angle and the ellipticity of the probe polarization after the filament–because of the pump-induced birefringence. That means at a certain probe polarization rotation angle, it will have the fixed ellipticity of the probe polarization. It happens both after the pump-produced filament and inside the filament when the probe pulse co-propagates with the pump pulse. Here we emphasize that even if we vary the angle between the initial pump and probe polarizations, the probe's dephasing ε always yields roughly the same values, since the value of dephasing ε depends only on the non-linear refractive index of argon and the integral of the pump clamped intensity over the interaction length. Indeed, the clamped intensity variation along the filament depends neither on the pump linear polarization direction nor on the probe polarization. The former is due to the initial isotropy of argon, the latter is due to the negligible effect of the probe on the pump during the propagation. That means if we replace argon by some unknown isotropic molecular gas, we can retrieve the XPM-induced refractive index change Δn^{XPM}_{probe} in this gas by applying Eq. (3.3.1) to the dephasing ε and the filament length obtained in the experiment.

Figures 3.2(a, b, c) illustrate that after interaction with the pump, for pairs of probe polarizations set at angles ψ_{probe} = 45°$\pm\alpha$ [Fig. 3.2(d)] the resultant elliptical polarizations rotate through the same angle from its initial position towards opposite directions. The symmetry of the rotation originates from the constant dephasing (ε) between the two components of the probe polarization. This symmetry can be seen from Eq. (3.3.4) which gives

$$\tan 2(\psi_{probe} + \phi) = \frac{2|E_{2\omega x}||E_{2\omega y}|}{|E_{2\omega x}|^2 - |E_{2\omega y}|^2}\cos\varepsilon = \frac{2\sin\psi_{probe}\cos\psi_{probe}}{\cos^2\psi_{probe} - \sin^2\psi_{probe}}\cos\varepsilon = \tan 2\psi_{probe} \times \cos\varepsilon \tag{3.4.1}$$

For angles like ψ_{probe}=45°±α, since ε keeps constant, the term ($\tan 2\psi_{probe} \times \cos\varepsilon$) at the right side of Eq. (3.4.1) will have the same magnitude but the opposite sign; let's put

($\tan 2\psi_{probe} \times \cos\varepsilon = \pm\beta$). From Eq. (3.4.1), we get $\phi = -\psi_{probe} \pm \frac{\tan^{-1}\beta}{2}$, which means the same polarization rotation angles towards opposite directions from the initial probe direction.

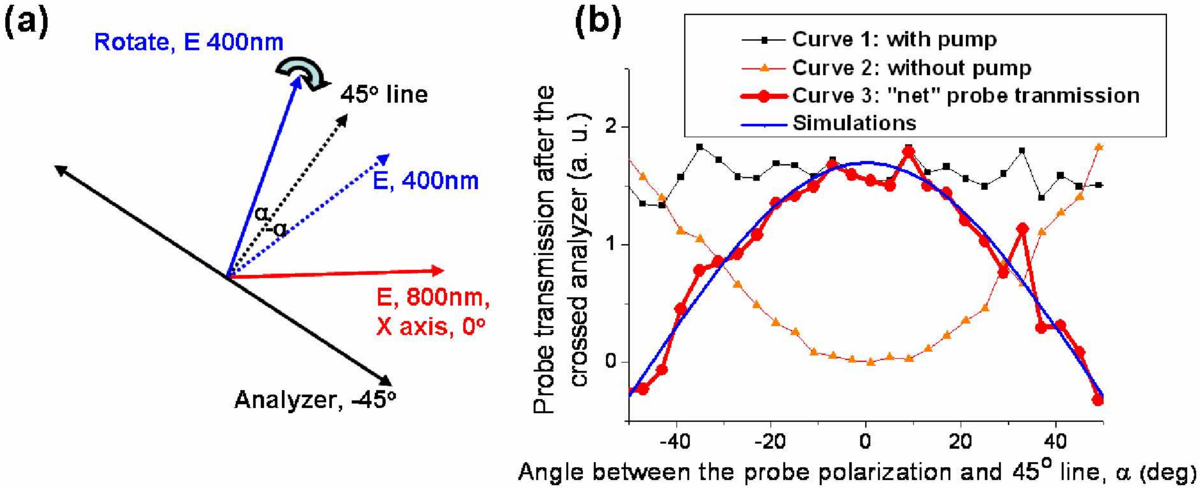

Fig. 3.3 (a) Polarization scheme of the pump, probe and analyzer. In (b), probe energy, integrated over the whole transmitted probe beam pattern is shown as a function of the probe polarization angle ψ_{probe}, when pump was turned on (curve 1; black squares, solid curve) and off (curve 2; orange triangles, solid curve). Their difference which means the XPM induced probe transmission is shown in curve 3 (red circles, solid curve, curve 1 minus curve 2) and fitted by cosine square.

In order to have a more complete physical picture of the birefringence induced rotation of the probe due to filament guiding [100] and electronic XPM, two supplementary experiments were carried out by fixing the polarization of the pump and rotating the probe and vice versa while measuring the probe transmission through the fixed analyzer. The first is to rotate the probe. In Fig. 3.3(a), we define the experimentally fixed pump polarization as our x axis, which is set at 45° to the fixed transmission axis of the analyzer. By rotating the polarization of the probe, we measured the probe transmission after the analyzer, at various positions of α and $-\alpha$ symmetrical about the 45° line. Each point in Fig. 3.3(b) was obtained by integrating the whole probe beam pattern on the paper screen imaged onto the CCD camera as the angle α changes from -45° to 45°. Since the transmission axis of the analyzer was fixed, rotating the probe polarization will vary the transmitted probe energy. Curves 1 (total transmission) and 2 (background) in Fig. 3.3(b) were taken as the pump was turned on and off, respectively. The XPM-induced probe transmission as a function of angle α was depicted by curve 3 in Fig. 3.3(b) by removing the background from the total transmission of the probe (curve 1 minus curve 2). In this measurement, the XPM-induced probe pulse transmission reaches a maximum at α = 0° and shows equal values at the symmetrical pairs of angles ($\alpha\,;-\alpha$) around the maximum. The equal values at the symmetrical pairs of angles ($\alpha\,,-\alpha$) matches well with that on Figs. 3.2(a, b, c); i.e. the pairs of probe polarization angles, $45^{\circ}\pm\alpha$, rotate through the same angles towards opposite directions after interacting with the pump.

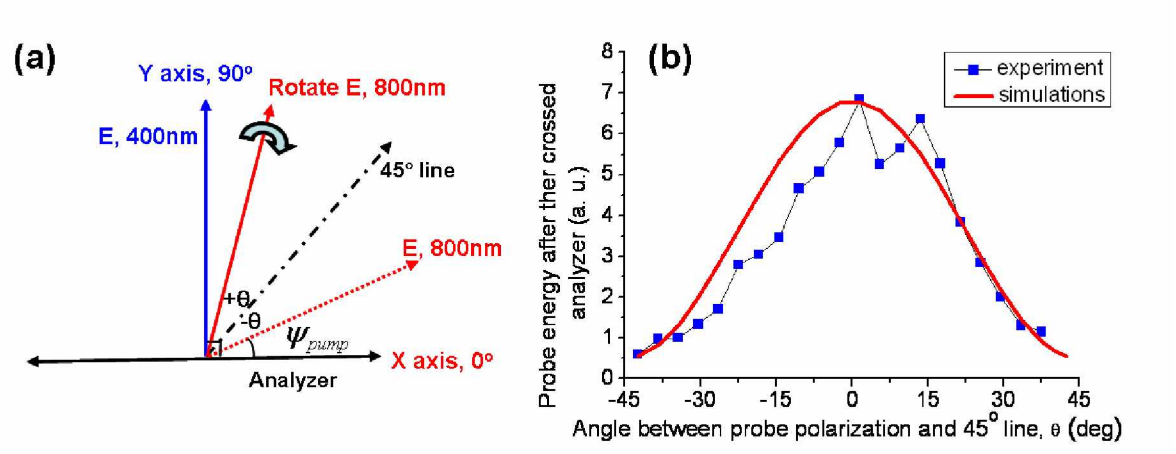

Fig. 3.4 (a) Illustration of pump and probe polarization in the primed coordinate system. (b) The experimentally obtained probe transmission through the crossed analyzer for the pairs of angles θ and $-\theta$. Here we use $\cos^2 2\theta$ to fit.

The second experiment is to rotate the pump polarization with the probe and analyzer fixed. The scheme is shown in Fig. 3.4(a). We define the experimentally fixed transmission axis of the analyzer as our x axis (0°) which is crossed by the fixed probe polarization (90°). θ is the angle between the pump polarization direction and the 45° line. By rotating the pump polarization about the 45° line symmetrically through the angle $\pm\theta$, the probe transmission through the analyzer integrated over the whole beam pattern was recorded. The results are shown in Fig. 3.4(b). Similar to Fig. 3.3(b), the transmitted probe after the analyzer also gives a maximum when the pump polarization is rotated to the 45° line (θ = 0°) and yields equal values at the symmetrical pairs of angles. This effect can be simply understood by considering the projection of the transmitted probe polarization on the x-axis through XPM:

$$P_{2\omega x}^{(3)} = \chi_{xxxx}^{(3)} E_{2\omega x} E_{\omega x} E_{\omega x}^{*} + \chi_{xxyy}^{(3)} E_{2\omega x} E_{\omega y} E_{\omega y}^{*} + \chi_{xyxy}^{(3)} E_{2\omega y} E_{\omega x} E_{\omega y}^{*} + \chi_{xyyx}^{(3)} E_{2\omega y} E_{\omega y} E_{\omega x}^{*}\,. \qquad (3.4.2)$$

While taking into account the experimental condition for the initial probe polarization $E_{2\omega x} = 0$, we have

$$P_{2\omega x}^{(3)}(2\omega) = \chi_{xyxy}^{(3)} E_{2\omega y} (E_{\omega y} E_{\omega x}^{*} + E_{\omega y}^{*} E_{\omega x}) = \chi_{xyxy}^{(3)} E_{2\omega y} \left| E_{\omega} \right|^2 \sin 2\psi_{pump} = \chi_{xyxy}^{(3)} E_{2\omega y} \left| E_{\omega} \right|^2 \cos(2\theta) \tag{3.4.3}$$

since $\chi_{xyxy}^{(3)} = \chi_{xyyx}^{(3)}$ and $\psi_{pump} = \theta + 45^{o}$. As shown in Fig. 3.4(b), the experimental curve fits well with the curve $y = \eta \cos^2 2\theta$, originating from Eq. (3.4.3) while η is a constant for normalization.

3.5 Discussion and conclusion

We experimentally demonstrated an optical gating technique for quantitative ultrafast birefringence measurement in an atomic gas. By simply measuring the filament-induced polarization rotation of a probe pulse, we can easily and quantitatively obtain the ultrafast birefringence caused by filament guiding and cross phase modulation. This technique can be used in atomic gases. In molecular gases, the same technique at proper delays could measure the birefringence as a result of molecular rotation through Raman-type excitation as well as the birefringence of the rotational wave-packet at various revival times. This type of measurement could be applied to remote sensing of molecular gas targets because they possess not only different revival times but also different and unique birefringence at proper delays, opening new perspectives for ultrafast information processing and telecommunication.

Chapter 4 Polarization evolution in the wake of molecular alignment inside a filament

4.1 Introduction

Filamentation induced birefringence in isotropic gas media has attracted increasing attention owing to its remarkable effects on the spatial and spectral reshaping of a probing pulse [66, 99, 108-111]. In atomic gases, the ultrafast birefringence was quantified by measuring the filament-induced polarization change of a probe pulse [66, 99, 102]. In molecular gases, in particular for linear molecules, besides this instantaneous electronic response, a delayed birefringence was induced by the molecular alignment and revivals. The molecular alignment induced birefringence could be measured by means of the weak-field probe polarization technique with 45° between the initially linearly polarized pump and probe [45] or by making use of the spatial cross-defocusing effect of the probe pulse through fixing the pump and probe polarization crossed with each other [106,107]. In the former case, a filament was demonstrated to be a polarization separator, with the parallel-to-pump polarization component guided along the propagation axis [68,100,101].

Due to birefringence, instantaneous or delayed, through propagation, the probe nonlinear phases along and perpendicular to the pump polarization directions are accumulated separately over the interaction length. The phase difference at the output would give rise to an elliptic probe polarization. P. Béjot *et al.* [99] has elaborated the pressure (dephasing) dependence of the polarization diagram of a probe beam driven by an ultrashort laser filament in argon cell, with an initial angle of 45° between the linear polarizations of the pump and the probe. However, detailed measurement for the response of the probe polarization states caused by molecular alignment induced delayed birefringence has been left aside to date. In this chapter, the evolution of the polarization states of the output probe is specified at the revivals of molecular N_2, by measuring the probe elliptical polarization states under various relative delays between the pump and probe pulse. The rotation angle of the main axis of the output probe at molecular revival follows well with our simulations.

4.2 Experiment setup

The experimental setup is similar to that described in Fig. 3.1(a) in chapter 3. A single 1-cm-long filament was created by focusing a 0.6 mJ, linearly polarized, 40 fs, 800nm laser pulse in 1 bar of nitrogen with a lens (f = 50 cm). The filament was probed by a second linearly polarized, weak pulse (40 fs, 0.8 μJ, 400 nm). After the filament, a dichroic mirror was used to block the pump beam while transmitting the probe. The probe pulse was analyzed by a polarizer and the resulting transmission was projected on a white paper screen. A CCD camera with a bandpass filter centered at 400 nm (bandwidth = 80 nm) in front of it was used to detect the probe scattering from the paper [66, 68]. The experiment was done by imaging the probe scattering while rotating the transmission axis of the analyzer at different relative delay between the pump and the probe.

4.3 Theoretical model

In this paper, we assume that the propagation wave vectors are in the z direction and the pump linear polarization is along the x direction (0^o). For molecular alignment induced birefringence of the probe pulse, in the case of linear molecules having two principal polarizabilities equal and the third one larger ($\alpha_x=\alpha_y< \alpha_z$), the modulation of the refractive indices along (δn_X^{align}) and perpendicular (δn_Y^{align}) to the laser field are given by [21, 65]

$$\delta n_X^{align}(r,t) = \frac{2\pi N}{n_0}\Delta\alpha(<\cos^2\theta>_t -1/3) \tag{4.3.1}$$

$$\delta n_Y^{align}(r,t) = -\frac{\pi N}{n_0}\Delta\alpha(<\cos^2\theta>_t -1/3) \tag{4.3.2}$$

where N and n_0 denote the molecular number density and linear refractive index of the initially randomly aligned molecules. $\Delta\alpha$ is the molecular polarizability anisotropy, θ is the angle between the laser polarization and the molecular axis and $< >_t$ is the time-dependent ensemble average [21, 65, 68, 101]. t is the retarded time between the pump and probe pulses. The laser-induced plasma defocusing has no preference along and perpendicular to the laser field, thus the resulting birefringence $\Delta n^{align}(r,t)$ can be expressed as

$$\begin{aligned}\Delta n^{align}(r,t) &= (\delta n_X^{align}(r,t) + \Delta n_{plasma}(r,t)) - (\delta n_Y^{align}(r,t) + \Delta n_{plasma}(r,t)) \\ &= \delta n_X^{align}(r,t) - \delta n_Y^{align}(r,t) = \frac{3\pi N}{n_0}\Delta\alpha(<\cos^2\theta>_t - 1/3)\end{aligned} \tag{4.3.3}$$

The alignment induced birefringence $\Delta n^{align}(r,t)$ is proportional to $(<\cos^2\theta>_t - 1/3)$. The simulated statistic metric $(<\cos^2\theta>_t - 1/3)$ for N_2 molecules is shown in Fig. 4.1(a), with the parameters expressed according to the experimental conditions: gas temperature T=21°C, the peak intensity of the aligning field I=5×10^{13} W/cm^2 and its FWHM duration t=40 fs. Fig. 4.1(b) illustrates the revival of the pre-aligned N_2 molecules, which is experimentally measured using the weak field polarization technique [45]. By varying the retarded time between the pump and the probe, the x and y axes become fast and slow axis alternately. For randomly oriented molecules, the revival signal $<\cos^2\theta>$ =1/3 and the birefringence $\Delta n^{align}(r,t)$=0, which makes the probe projections along (x axis, 0°) and perpendicular (y axis, 90°) to the field polarization travel with the same speed. When the molecular orientation tends to be parallel to the field polarization of the pump (in-phase revivals in Fig. 4.1(a)), $<\cos^2\theta>$ >1/3 and $\Delta n^{align}(r,t)$>0 (Eq. (4.3.3)). In this case, the x component of the probe propagates slower than the y component, whereas the perpendicular orientation (off-phase revival in Fig. 4.1(a)) indicates $<\cos^2\theta>$ <1/3, $\Delta n^{align}(r,t)$<0, and the x component is having a higher speed. (Note: v=c/n)

Due to the molecular alignment induced birefringence, integrated over the whole interaction length (roughly the length of the filament), the probe nonlinear phases along the 0° and the 90° axes are accumulated separately over the interaction length. By approximating the filament as a uniform cylinder of length L, the overall dephasing $\varepsilon(t)$ accumulated between the probe components along the 0° and the 90° axes is given by [65]:

$$\varepsilon = \Delta n^{align}\omega_0 L / c_0 = \frac{3\pi N\omega_0 L}{n_0 c_0}\Delta\alpha(<\cos^2\theta>_t - 1/3) = \eta(<\cos^2\theta>_t - 1/3), \tag{4.3.4}$$

where ω_0 is the laser central angular frequency; c_0 is the speed of light in vacuum and $\eta \sim \frac{3\pi\Delta\alpha N\omega_0 L}{n_0 c_0}$ is a constant. The alignment induced dephasing $\varepsilon(t)$ is proportional to $(<\cos^2\theta>_t - 1/3)$.

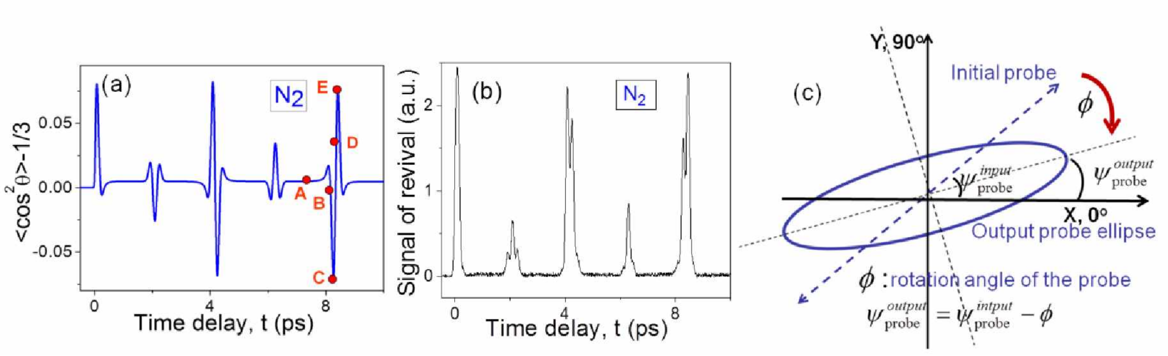

Fig. 4.1 (a) The calculated revival for molecular N_2 $(<\cos^2\theta> -1/3)$ along the field polarization of the probe pulse. (b) Experimentally measured molecular alignment signal of N_2. (c) The polarization scheme for the probe.

As the time delay between the pump and probe varies, the probe pulse will see different birefringence $\Delta n^{align}(t)$, giving rise to the polarization rotation of the probe and making the initially linearly polarized probe elliptical [66,99,102]. A laboratory coordinate system shown in Fig. 4.1(c) is used to describe the two components of the probe field along the x and y axes:

$$E_x' = E_x \cos(\omega t - kz), \tag{4.3.5}$$

$$E_y' = E_y \cos(\omega t - kz + \varepsilon), \tag{4.3.6}$$

where E_x and E_y as the initial electrical field of the probe projected along (0°, x axis) and perpendicular (90°, y axis) to the pump polarization direction, while E_x' and E_y' are the output ones. Under the plane wave assumption, the rotation angle and the ellipticity of the probe polarization can be expressed as [66]:

$$\tan 2(\psi_{probe}^{input} - \phi) = \frac{2E_x E_y}{E_x^2 - E_y^2} \cos\varepsilon \tag{4.3.7}$$

$$\psi_{probe}^{output} = \psi_{probe}^{input} - \phi \tag{4.3.8}$$

where $\psi_{probe}^{input} = \arctan(|E_y| / |E_x|)$ is defined as the angle between the initial linear polarization of the probe and that of the pump (0°, x axis). Throughout this paper, we call it initial polarization of the probe, which is set between 0° and 90° by the chosen coordinate system. ψ_{probe}^{output} is defined as the output polarization of the probe, which is actually the angle between x axis and the major axis of the output probe polarization ellipse, and $\phi = \psi_{probe}^{input} - \psi_{probe}^{output}$ is the polarization rotation angle [see Fig. 4.1(c)]. ϕ is positive, when the final polarization direction of the probe rotates clockwise from the initial one with the observer looking into the probe propagation direction.

The theoretical calculation is done by applying the de-phasing $\varepsilon(t) = \dfrac{3\pi\Delta\alpha N\omega_0 L}{n_0 c_0}(<\cos^2\theta>_t - 1/3)$ into Eq. (4.3.7), in order to retrieve the rotation angle ϕ (t) of the probe. The parameters are faithfully chosen according to the experimental conditions: polarizability anisotropy of $\Delta\alpha_{N2} = 0.93\times10^{-24}$ cm^3 [21], interaction length L=1.3 cm, and molecular number density $N_{N2}=2.5\times10^{19}$ cm^{-3}, with the theoretical revival of N_2 $(<\cos^2\theta>_t - 1/3)$. The result of the theoretical calculation of the rotation angle ϕ(t) of the probe is shown as the black curve in Fig. 4.3.

4.4 Results and discussion

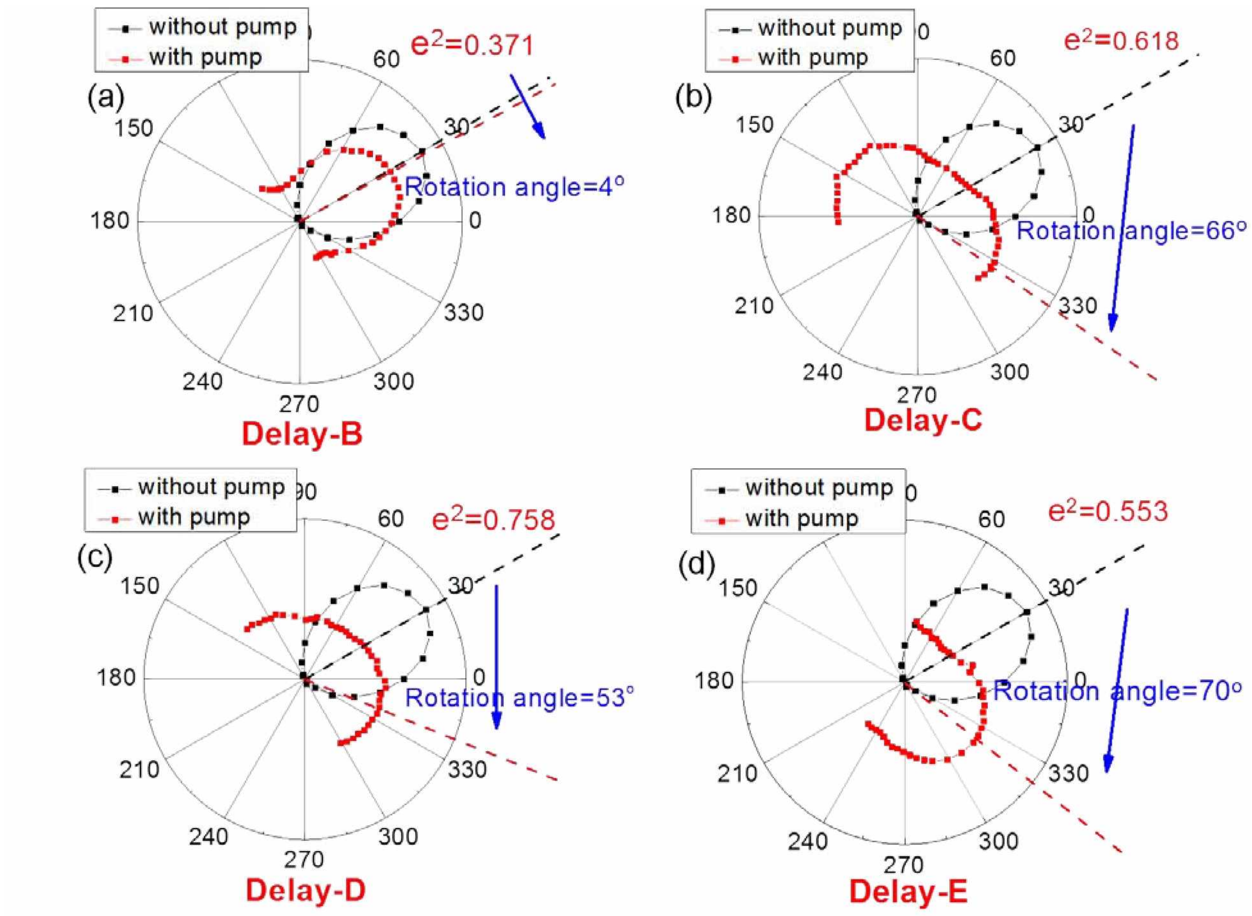

Fig. 4.2 (Color online) Polarization analysis of the transmitted probe in the wake of the pump for initially 30° between the pump and probe polarization directions at different delay positions as labeled in Fig. 4.1(a). Black-dotted lines correspond to probe polarization state at delay-A in Fig. 4.1(a), while the red-dotted lines correspond to probe polarization state at delay B-E in Fig. 4.1(a). Black dash line is at 30° and red dash lines indicate the main axis of the probe polarization.

In order to investigate the polarization states of the probe developing with different orientations of N_2 molecule, the experiment was carried out by rotating the transmission axis of the analyzer at different pump-probe delay while measuring the probe transmission. We scanned the pump-probe delay over the full range of N_2's molecular revival. As an example, we show one set of the polarization changes ϕ of the probe around the full revival region (around 8 ps in Fig. 4.1a) when the molecules evolve from being perpendicular to the pump linear polarization to being parallel and back. This evolution is compared with the probe polarization state when the molecules are randomly oriented. The polarization direction of the initially linearly polarized probe was fixed at 30° with respect to that of the pump (0°) ($\psi_{probe}^{input} = 30°$). The probe polarization states around the full revival at time delays B,C,D,E as labeled in Fig. 4.1(a) are shown in Figs. 4.2a-d (red curve) as compared to the probe polarization state (black curve) at delay A in Fig. 4.1(a). Delay A is for random orientation of the molecules which is equivalent to the initial polarization of the probe; delays B-E give the evolution of the molecules from perpendicular to parallel. In Figs. 4.2a-d, the rotation angle is the angle between the initial probe polarization direction (30^o) and the final direction for the major axis of the probe ellipse. The measured ellipticity square e^2 is the ratio between the length of the minor axis and that of the major axis on the experimentally measured angular transmission. (Note that e is defined as the ratio of electric field amplitudes of the ellipse while the transmission corresponds to the transmitted energy of the probe which is proportional to the electric field squared.) We compare the probe polarization states for various states of molecular alignment (red curve in Figs. 4.2a-d) with the one corresponding to randomly distributed molecules (black cure in Figs. 4.2a-d). We see that after propagating through the alignment region in the wake of the pump, the probe polarization integrated over the whole beam became elliptical, with the major axes rotating clock-wise with the observer looking into the probe propagation direction.

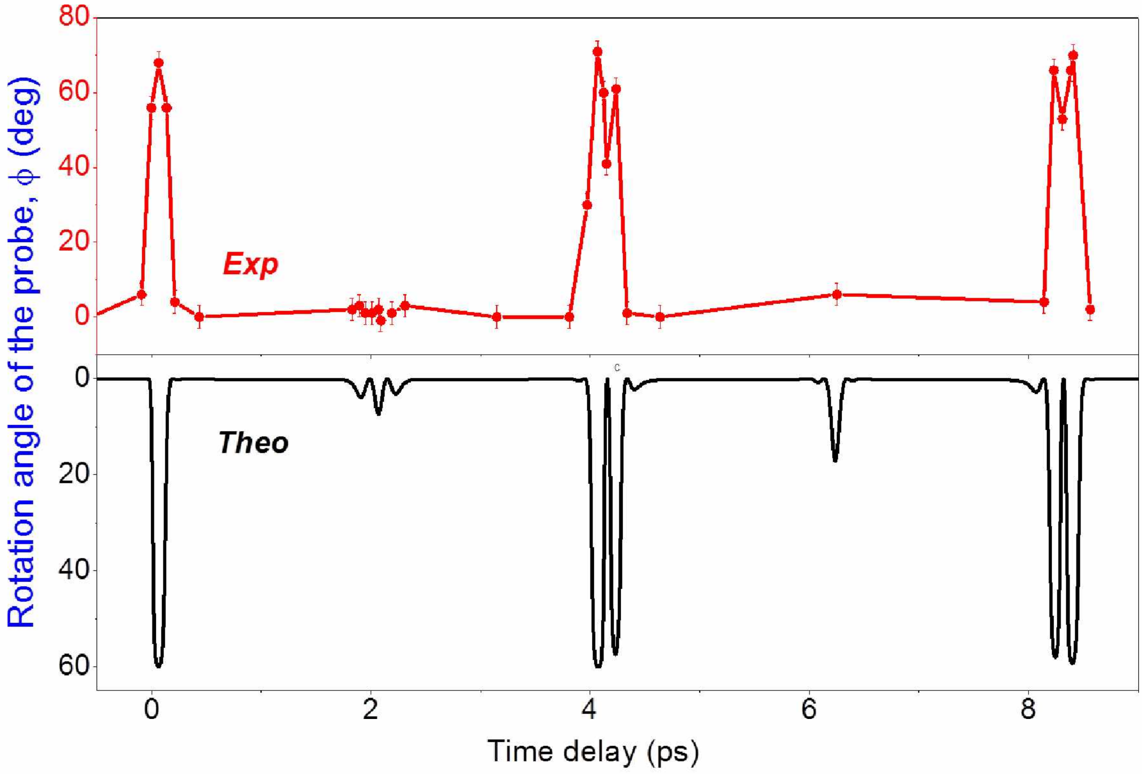

Fig. 4.3 Rotation angle of the major axis of the probe elliptical polarization (red circle, solid line) as a function of the relative delay between pump and probe. Numerical simulation (black curve, inverted for clarity) of Eq. (4.3.7) at 296 K for a Gaussian pump envelope of 70 fs pulse duration.

The rotation angles ϕ of the polarization direction of the probe as a function of delay over the full range of revivals are summarized in Fig. 4.3 (red circle, solid line), which is well reproduced by the simulations (black curve). The theoretical calculation is done by applying the de-phasing $\varepsilon(t)=\frac{3\pi\Delta\alpha N\omega_0 L}{n_0 c_0}(<\cos^2\theta>_t -1/3)$ into Eq. (4.3.7), with similar parameters as those of the experimental condition.

4.5 Conclusion

We experimentally measured the probe elliptical polarization states at revivals of N_2 molecules. By analyzing the detailed response of the polarization states of the probe induced by the molecular alignment, we discovered that the rotation angles for the main axis of the output probe at different time delays follows the revival of molecular N_2.

Chapter 5 Filament-induced lasing action[2]

5.1 Introduction

The propagation of intense femtosecond near-infrared laser pulses in the atmosphere has been the subject of interest both experimentally and theoretically during the last few years [1-6]. For short filament (< 5cm), intensity clamping produces self-stabilized high peak intensity inside the filament of the order of ~5 × 10^{13} W/cm^2, while longer filaments might lead to intensity spikes [112, 113]. Both of them can be beneficial for a lot of nonlinear effects, such as remote sensing [24-27], molecular alignment [43-46], harmonic generation [51, 112-114], etc. Inside filament, molecules undergo mutiphoton/tunneling ionization and fragmentation, which excites the ions and fragment molecules into some highly excited states, resulting in the emission of characteristic fingerprint fluorescence [41, 42].

Q. Luo et al. [11] have observed that the spontaneous emission from N_2 molecules and ions become amplified as it propagates back along the filament. The amplified spontaneous emission (ASE) is characterized as ASE lasing. More recently, lasing action from filaments was shown to operate at both ~391 and 337 nm in molecular nitrogen [20, 69] and at ~845 nm in atomic oxygen [115]. In this work, we investigated the backscattered fluorescence of OH from water vapor in air, from the filament which is generated by a femtosecond Ti:sapphire laser pulse. The dependence of the fluorescence of OH on the filament length shows clear evidence of ASE. Besides, by measuring the intensity inside the filament and fluorescence intensity of OH, a high degree of nonlinearity is obtained.

---

[2] The results presented in this chapter are based on the following article. S. Yuan, T. J. Wang, Y. Teranishi, A. Sridharan, S. H. Lin, H. P. Zeng and S. L. Chin, "Lasing action in water vapor induced by ultrashort laser filamentation", Appl. Phys. Lett. 102 224102 (2013).

5.2 Experimental setup:

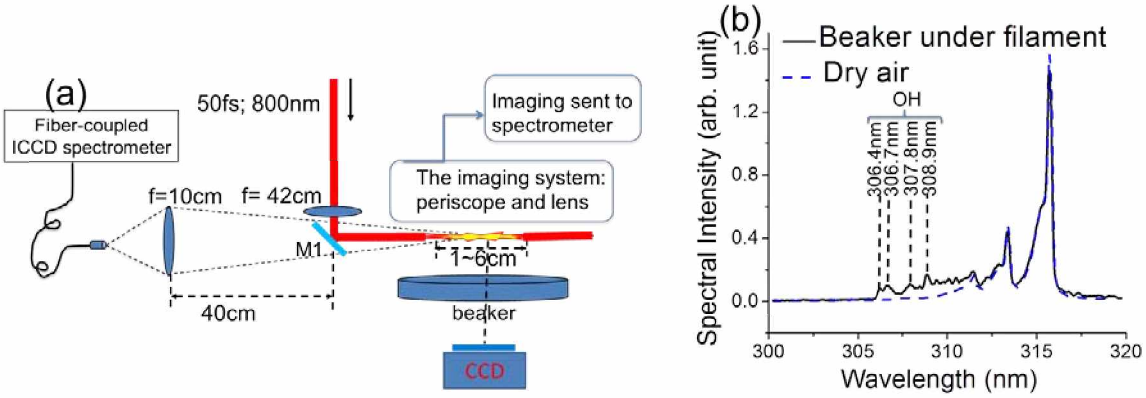

Fig. 5.1. (a) Schematic layout of experimental setup and (b) typical spectrum in the range of 300-320nm for filament-induced fluorescence of water vapor in air. The spectrum was taken at room temperature of 22 ℃ and filament-to-water surface of 4mm.

The experiments were done by using a 12 mJ/50 fs, 10 Hz Ti:Sapphire laser beam. The schematic of the experimental setup is illustrated in Fig. 5.1(a). The laser beam was focused by a lens of 42 cm focal length. A dichroic mirror (M1, 7.5 cm in diameter) with high reflectivity at 800 nm and 50% transmission from 300 nm to 315 nm was used right after the lens to reflect the beam at 45° incidence angle. A 5-cm-long filament was created roughly 35 cm after the mirror (M1) in air. A beaker with open area of 15 cm in diameter was placed 4 mm under the filament. The beaker was fully filled with distilled water, in order to create an environment with a water vapor concentration of ~ 2% at room temperature (22°C) according to our measurement in ref. 38. The backscattered fluorescence from the filament zone was collected after the dichroic mirror (M1) with a fused-silica lens (5.08 cm in diameter, 10 cm focal length) and sent to an ICCD-gated spectrometer (Acton Research Corporation, SpectraPro-500i) through a fiber coupler. The fluorescence from the side was obtained by imaging the filament onto and parallel to the 100 μm-wide slit of the same ICCD-gated spectrometer using two identical fused-silica lenses (ϕ = 5.08 cm f = 10 cm) and one periscope. A grating of 1200 grooves/mm (blazed at 500 nm) was used. All the results shown in this paper are averaged over 1000 laser shots.

5.3 Experimental results and discussions:

Fluorescence coming from the water vapor was found in the range of 306-309 nm as shown by the black curve in Fig. 5.1(b), at room temperature (22°C) and with 2 mJ of the pump pulse energy. The fluorescence was identified as OH* radiation from $A^2\sum^+ \to X^2\Pi$ [38,116]. The fluorescence from molecular N_2 was also observed around the peak of 315 nm as shown in Fig.

5.1(b). To check whether the fluorescence of N_2 has any effect on the typical OH radiation at 308.9 nm, another trial experiment was carried out. The beaker filled with water was replaced by a gas nozzle, which continuously provided a dry air blow to reduce the amount of water vapor in air. The spectrum of the back-scattered fluorescence from the filament was then detected. The result is shown as the blue dashed curve in Fig. 5.1(b). In this case, the signal around 308.9 nm which corresponds to the OH fluorescence decreases to the noise level; i.e. both N_2 and O_2 molecules have no contribution to the fluorescence of OH around 308.9 nm. In this paper, the spectral peak intensities of 308.9 nm from OH were chosen as the OH fluorescence.

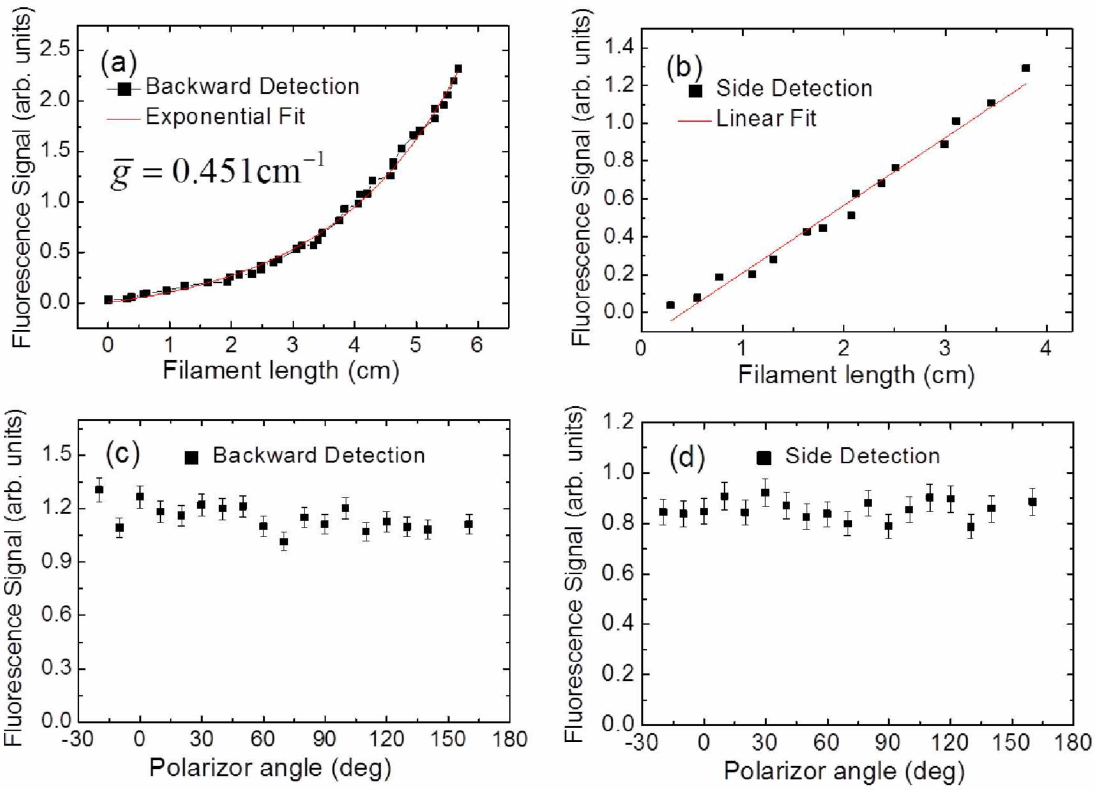

Fig. 5.2 The fluorescence intensity of OH at 308.9 nm versus the filament length. The fluorescence is recorded in backward (a) and side (b) direction. The laser beam is focused by an external focusing lens (f = 42 cm). The solid line in (a) is the gain curve calculated with Eq. (5.3.1 (a)). The polarization property of the fluorescence in backward and side direction is shown in (c) and (d), respectively.

The OH fluorescence in the backward and side directions was measured with the gated-ICCD spectrometer under different input pump pulse energy. A CCD was employed to image the filament from the side [see Fig. 5.1(a)] in order to measure the length of the filament. The result is shown in Fig. 5.2(a) (detected from the backward direction) and Fig. 5.2(b) (detected from the side). In Fig. 5.2(a), the backscattered OH fluorescence increases exponentially as the filament length increases, while in Fig. 5.2(b), the OH fluorescence from the side has a linear dependence with the filament length. If the OH fluorescence signal is incoherent, OH fluorescence emission detected in the backward and side directions should give similar results. However, in our experiment, the on-axis backward OH fluorescence signal increases much faster (increase exponentially) with the filament length than the one detected from the side (increase linearly). This indicates amplified spontaneous emission. The ASE can be expressed as:

$$I \propto P = \int_0^L P_s e^{g(l)l}\,dl = \begin{cases} \frac{P_s}{\bar{g}}(e^{\bar{g}L} - 1) & (5.3.1a) \\ & (with\ amplification) \\ \frac{P_s}{\bar{g}} \times \bar{g}L = P_sL & (5.3.1b) \\ & (when\ \bar{g}L \ll 1) \end{cases}$$

where I is the intensity of the spontaneous emission, P the spontaneous emission power, P_s the spontaneous emission power per unit length, L the effective length of the gain medium, which roughly equals to the length of the filament. $g(l)$ is defined as the optical gain coefficient, which is a function of the relative position l inside the filament. $\bar{g}$ is the effective gain coefficient over the filament length. In our experiment, the maximum length of the filament is 5 cm. In this sense, due to intensity clamping, we assume the intensity inside the filament is uniform and consider the filament zone approximately as a cylinder, meaning that the optical gain $g(l)$ has little deviation from the effective gain coefficient $\bar{g}$ over the filament length. In Eq. (5.3.1a), when the spontaneous fluorescence is amplified along the gain medium, the integrated fluorescence shows an exponential dependence with the length L of the gain medium (filament), which corresponds to the result in Fig. 5.2(a). By applying Eq. (5.3.1a), the experimental curve in Fig. 5.2(a) can be fitted with an effective gain coefficient of 0.451 cm^{-1}. In Fig. 5.2(b), the OH fluorescence is proportional to the filament length, since the fluorescence detected from the side only sees the gain along the very small filament cross section (roughly 100 μm), which is a short distance. The value of the gain along the cross section should have the same magnitude as the effective gain coefficient detected from the backward direction (0.451 cm^{-1}). Therefore, in this case the product of the gain (assuming $\bar{g} = 0.451 cm^{-1}$) and the length of the gain medium (L = 100 μm) is negligibly small ($\bar{g}L \ll 1$), which corresponds to Eq. (5.3.1b). As a result, the integrated OH fluorescence from the side is just the sum of the emission from all the small unit lengths along the filament, in accordance with our results in Fig. 5.2(b). The absolute value of the OH fluorescence intensities in Figs. 5.2(a) and 2(b) are not comparable, since the measurements from the side and the backward direction employed different techniques. The polarization of the fluorescence in the backward/side direction was measured by rotating a polarizer placed just before the fiber head (backward direction) or the slit of the spectrometer (side). Both of them are randomly polarized as shown in Figs. 5.2(c,d). The isotropic polarization and the difference between the gain in backward and side directions provide strong evidence for ASE lasing.

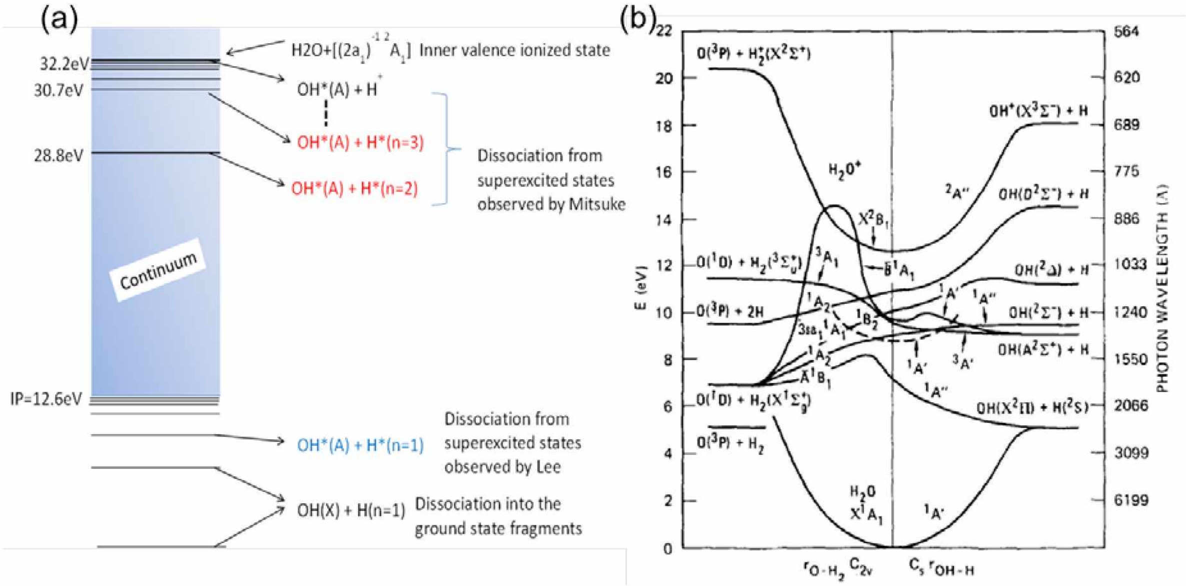

Fig. 5.3 (a) Schematic energy diagram for molecular H_2O. (b) Correlation diagram for the electronic states of H_2O relevant to the current observation. This diagram is given by Tsurubuchi [121]. The photon wavelengths corresponding to excitation energies are indicated. Fig. 5.3(b) is adapted with permission from [117] (1980AIP), image courtesy of Lee, SRI International, California.

In order to understand the physics of the lasing action and the dissociation process, an energy diagram was plotted and shown in Fig. 5.3(a), with 12.6 eV as the ionization potential (IP) of H_2O molecule. There are two distinctive dissociation channels for H_2O molecules below the ionization potential related to OH generation [117,118]: one dissociating into $H(^2S) + OH(X^2\Pi)$, giving rise to H and OH fragments in the ground states [118], and the other dissociating into $H(^2S)+OH(A^2\sum^+)$, resulting in H in the ground state and OH in the excited state. The threshold energy of 9.136 eV for exciting this channel comes from references [117-119] where single VUV photons were used in the dissociation of H_2O. The OH* fluorescence at 306-309 nm in this experiment was identified as the transition from $A^2\sum^+ \rightarrow X^2\Pi$ [38,116]. If the dissociation channels above the ionization potential (12.6 eV) happened, the excited state of H, named H*, would be generated together with OH*(A) [see Fig. 5.3(a)]. However, during the experiment, we did not observe any spectral line from the Balmer series, which corresponds to the H* radiation. Thus, it can be assumed that inside the filament the water vapor molecules can be dissociated through the channel $H(^2S) + OH(A^2\sum^+)$. The transition from OH ($A^2\sum^+ \rightarrow X^2\Pi$) emits fluorescence at 306-309 nm, having a peak at 308.9 nm.

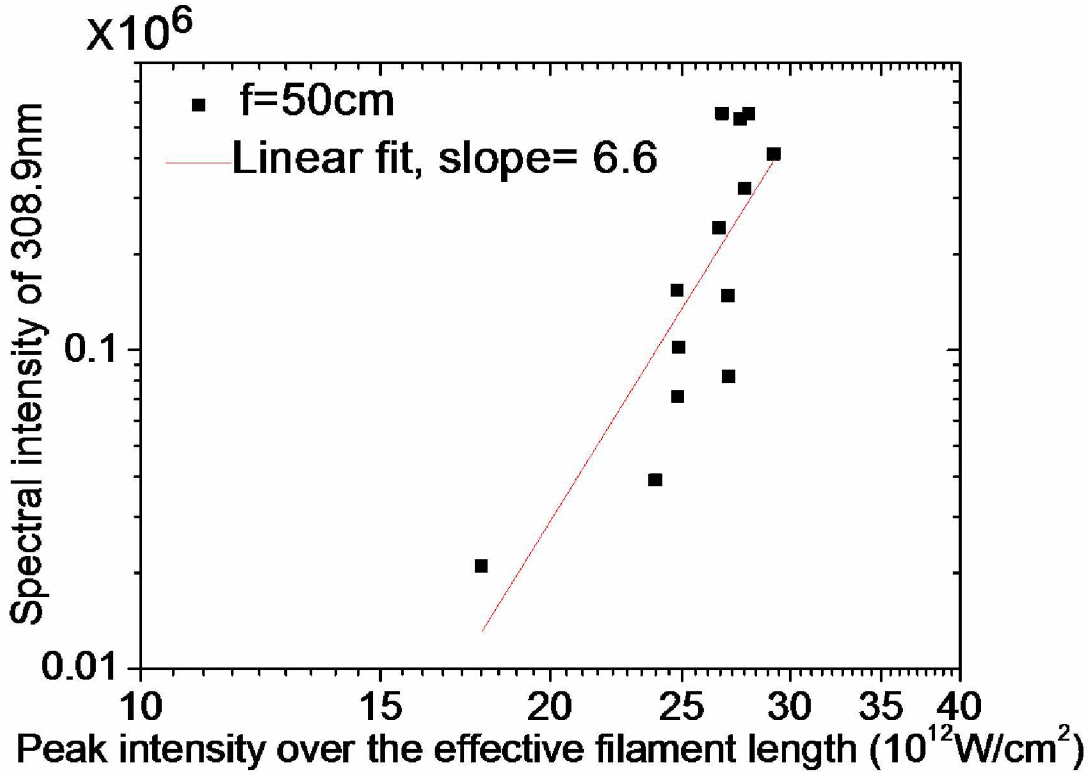

Fig. 5.4 Fluorescence intensities of OH 308.9 nm lines as a function of the peak intensity over the effective filament length, shown in log-log scale, with 50 cm focal length lens. The slope is 6.6.

In this sense, different from previous work that molecular H_2O is dissociated by single UV photon, the dissociation of H_2O molecule through $H(^2S) + OH(A^2\sum^+)$ by infrared photons at 800 nm is a mutiphoton or highly nonlinear field interaction process. In order to prove our assumption, one supplementary experiment was carried out by measuring the intensity inside the filament and OH fluorescence emission at different input pump pulse energies. Note that although the intensity is supposed to be uniform along the filament, if the pump power is below or near the critical power for self-focusing (~10 GW in air), the intensity inside the filament would change by varying the pump pulse energy. During this experiment, the lens f = 42 cm in Fig. 5.1(a) was replaced by another lens with f=50 cm. At different pump pulse energy, the effective filament length was imaged into the ICCD-gated spectrometer from the side. The intensity at every small unit lengths (0.15 mm by calibration) along the effective filament length was calculated according to Eq. (13) in [120], by measuring the ratio of the spectral intensity of two nitrogen fluorescence lines, 391 and 337 nm. Then the peak intensity was selected and the intensity of OH fluorescence at this unit length was recorded. We plotted the OH fluorescence versus the peak intensity over this unit length. The result is shown in a log-log plot in Fig. 5.4, with a slope of 6.6. The slope does not correspond to an exact number of photons. However, in Fig. 5.3(b) around 9 eV (roughly 6 times the photon energy) a high density of states exists. These states could be coupled by the strong field and dissociating into the $H(^2S) + OH(A^2\sum^+)$ channel. The fluorescence from $OH(A^2\sum^+)$ is attributed to the pumping to these excited states. The excitation probability into these coupled excited states may have the slope of 6 or 7 (or some other non-integer values). In this sense, the slope 6.6 which is observed in the experiment is the mixture of the contributions from various excited states.

Thus, it is reasonable to conclude that the gain in the fluorescence of OH comes from the dissociation channel $H_2O + nh\nu \rightarrow H(^2S) + OH(A^2\sum^+)$ [see Fig. 5.3(a)]. Here, n indicates the mixture of the contribution from various excited states and not an exact number of photons. However, if the other lower lying channel $H_2O + n'h\nu \rightarrow H(^2S) + OH(X^2\Pi)$ which would give rise to OH (X) fragments in the ground state were also possible, it would reduce the population inversion in the ensemble of OH population. We would argue that such latter channel would be less probable. Under strong broadband femtosecond laser field excitation, many molecular states might have been coupled by the field. The higher the density of states is, the more probable the coupling could be. In the experiment, the strong field was set by intensity clamping in the air filament where the intensity was of the order of 5×10^{13} W/cm^2. According to Fig. 5.3(b), the region of higher density of states is around 9 eV which would decay into the channel $H_2O + nh\nu \rightarrow H(^2S) + OH(A^2\sum^+)$. Hence, the excitation of this channel would be more probable. Since OH* is created directly, its population is naturally inverted, and thus ASE lasing occurs.

5.4 Conclusion:

In summary, an exponential variation of the backscattered fluorescence from water vapor with increasing filament length was experimentally observed. This indicates that the fluorescence has been amplified while it propagates back along the filament. It opens up possibilities for the investigation on lasing action of water vapor through filament, since it exhibits similar characteristics as the N_2 molecules and ions. For example, we might also expect that the harmonic-seeded remote laser emission [77] can be operated in water vapor molecules as well. Besides, different from previous work using UV pulse to dissociate molecular H_2O through single photon process, the molecular H_2O is dissociated by infrared pulse under strong field process inside a filament. The detailed underlying physics of the dissociation though filamentation awaits to be explored.

Chapter 6 Humidity measurement using filament-induced fluorescence spectroscopy[3)]

6.1 Introduction

Filamentation generated by high power, ultrafast pulse in the atmosphere has attracted a lot of scientific interest in recent years due to its applications such as sensing of chemical/biological agents [86,87,94,95], chemical reaction [125,126], photondissociation [82,115,123], forward and backward lasing [77,82,115,124], etc. Since the filament can be targeted at a long distance by adjusting the initial laser parameters, such as beam diameter, divergence, and pulse duration [1-5], remote sensing by filament induced breakdown spectroscopy has been demonstrated [14,26].

Kasparian et al. [14] have observed highly resolved atmospheric absorption spectrum from an altitude of 4.5 km, which opens the opportunity for aerosol identification in the atmosphere. Filamentation-assisted water condensation has been observed both in a cloud chamber and in the atmosphere [14,127,128]. For atmospheric physics, relative humidity is particularly important, because of its relevance to the changes of state of water content in air, which is also the key parameter for predicting the weather. Remote humidity measurements would indicate the water condensation condition in the atmosphere, which will help us understand the detailed physics in cloud formation or even lightning control [28]. Most recently, by Wang et al. [38] the absolute humidity was measured in air using filament-induced fluorescence spectroscopy. However, in that work [38] the humidity was calibrated by using the 308.9 nm fluorescence line from hydroxyl (OH) radical arising from laser induced dissociation of water vapor. The fluorescence from 308.9 nm is rather weak (two orders of magnitude weaker than nitrogen (N_2) fluorescence at 337.0 nm), and hence cannot be easily detected meters away.

---

[3] The results presented in this chapter are based on the following article: S. Yuan, T. J. Wang, H. P. Zeng and S. L. Chin, "Humidity measurement in air using filament-induced NH fluorescence spectroscopy", Appl. Phys. Lett. 104 091113 (2014)

6.2 Experimental setup

In this work, strong fluorescence emissions from NH free radical at 336 nm were found in air, by applying water vapor into an intense blue (400 nm) filament. A method based on femtosecond laser filaments induced chemical reaction is proposed to measure the relative humidity in air. The experimental results show that the fluorescence from NH free radicals is linearly dependent on the relative humidity in air. Besides, the amplified spontaneous emission (ASE) of NH radical in the backward direction was observed, which can extend the technique for remote fluorescence measurement.

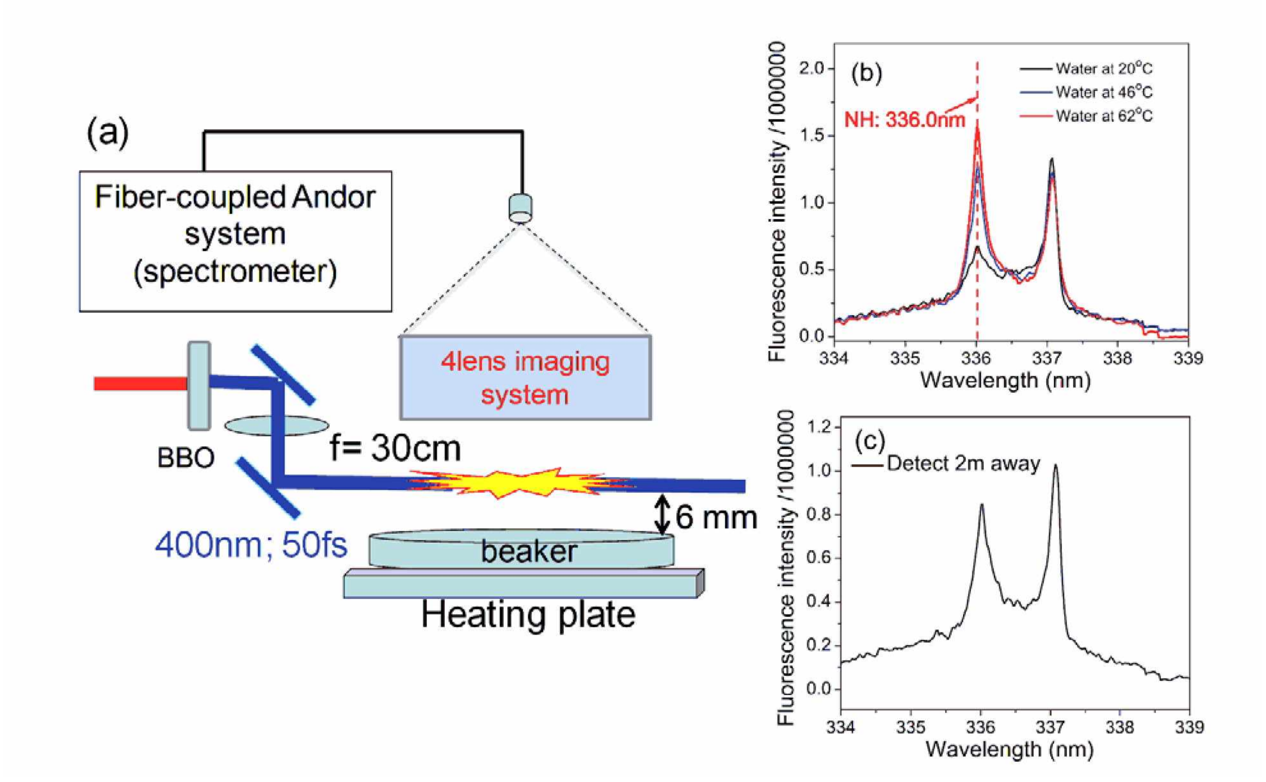

Fig. 6.1 (a) Schematic layout of experimental setup. Typical spectra in the range of 334-339 nm for filament-induced fluorescence of NH in air, with fluorescence collected at a distance of 50 cm (b) and 2 m (c) from the filament.

The experiments were done by using a 8 mJ/50 fs, 1 kHz Ti:Sapphire (800nm) laser beam. The schematic of the experimental setup is illustrated in Fig. 6.1(a). The laser beam passed through a 100-μm-thick BBO crystal for second harmonic generation, and was reflected by two dichroic mirrors with a high reflectivity of 99% at 400 nm and high transmission of 90% at 800 nm) to filter out the remaining 800 nm pulses. After that, the beam was focused by a lens of 30 cm focal length. The pulse energy at 400 nm is 1.8 mJ (measured after M2). A 3.5-cm-long filament was created. A beaker with open area of 10 cm in diameter was placed 6 mm under the filament. The beaker was fully filled with distilled water, which was used to change the relative humidity around the filament region. The water temperature was controllable by a heating plate underneath. The fluorescence from the side was collected at a distance of 50 cm from the filament by an imaging system of 4 fused silica lenses, and sent to an ICCD-gated spectrometer (Andor Michelle M5000) through a fiber coupler. All the results shown in this paper are averaged over 600 000 laser shots.

6.3 Results and discussions

Fluorescence at 336 nm was observed as shown in Fig. 6.1(b). The signal became stronger when the water was heated from 20 °C to 62 °C. The fluorescence was identified as NH radiation from $A\ ^3\Pi \rightarrow X\ ^3\Sigma^-$ [116,125]. The typical fluorescence from molecular N_2 at 337 nm was also observed as shown in Fig. 6.1(b). The structure of the NH spectral line is similar to that reported in [125], when filaments interact with a flame. Here, the NH radicals might be ascribed to the complicated recombination process of the dissociated N_2 and water vapor molecules. When the water temperature increases, the water vapor concentration goes higher so that the NH fluorescence gets stronger. Especially at 62 °C, the intensity of NH fluorescence at 336 nm is even stronger than that of N_2 fluorescence at 337 nm. "Clean" spectrum of NH was even found when the fluorescence was collected at a distance of 2 m from the filament, with water temperature at 43 °C and larger mirror for fluorescence collection [see Fig. 6.1(c)].

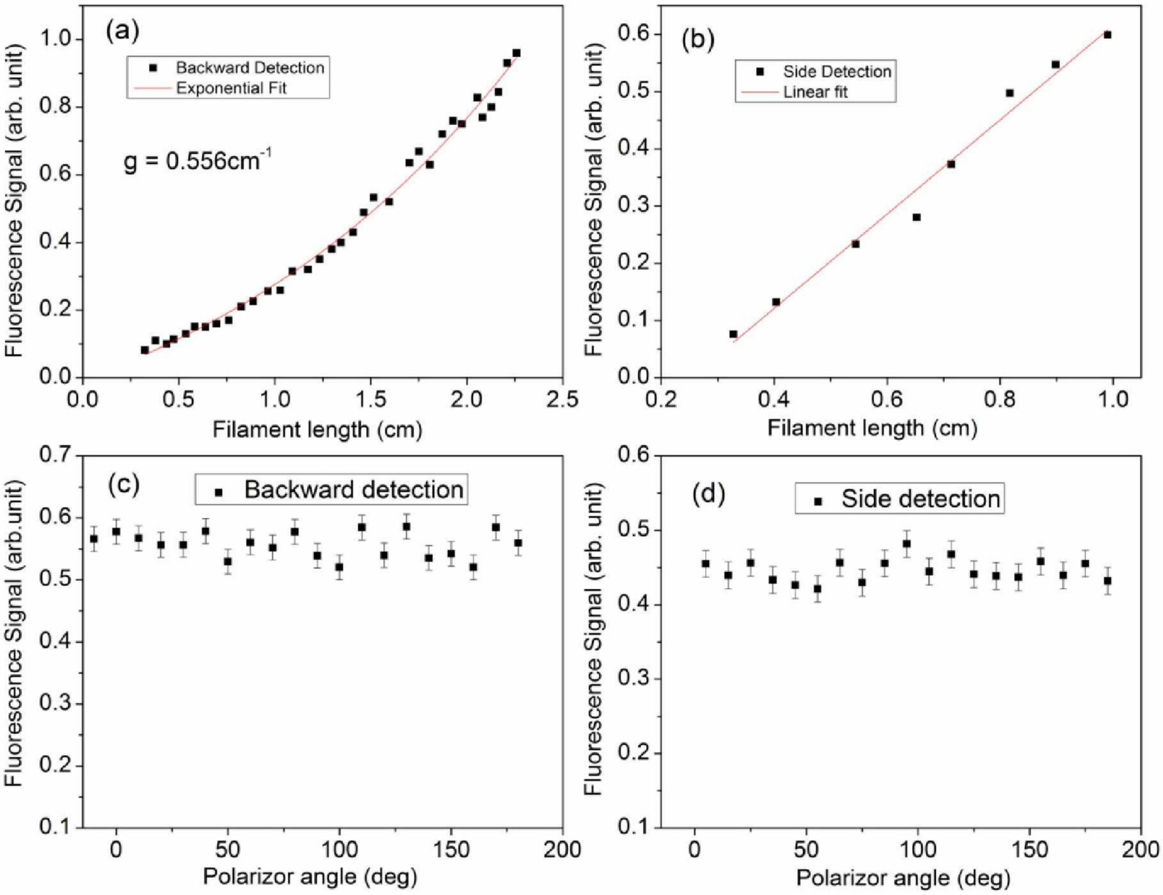

Fig. 6.2 The fluorescence intensity of NH at 336 nm versus the filament length. The fluorescence is measured in backward (a) and side (b) directions. The laser beam is focused by an external focusing lens (f = 37 cm). The polarization property of the fluorescence in backward and side directions is shown in (c) and (d), respectively.

In order to have a detailed physical picture of the filament-induced chemical reaction, the NH fluorescence in the backward and side directions were measured with the gated-ICCD spectrometer under different input pump pulse energy. The beam was focused by another focusing lens of 37 cm. The fluorescence from the side was measured by using the setup in Fig. 6.1(a). For detecting the backward fluorescence, one piece of dichroic mirror (fused silica, HR 95 % at 266 nm) with 70 % transmission at 400 nm and partially reflecting at 334 nm-339 nm was installed right after the mirror M2 in Fig. 6.1(a) with 45^{o} to the beam path, in order to transmit the 400-nm pump while reflecting the backward emitted fluorescence from the filament at 45^{o} incidence angle. A UG11 filter was also employed after the dichroic mirror to filter out the blue scattering from the surface of the mirror. The fluorescence was collected with a fused-silica lens with 8 cm focal length and then sent to the ICCD-gated spectrometer. The water temperature was fixed at 43 ^{o}C and the distance between the filament and the water surface was at 6 mm. We used a CCD to image the filament for measuring the filament length.

The result is shown in Fig. 6.2(a) and Fig. 6.2(b). In Fig. 6.2(a), the backward emitted NH fluorescence increases exponentially as the filament length increases, while in Fig. 6.2(b), the NH fluorescence from the side has a linear dependence with the filament length. If the NH fluorescence cannot see any gain effect along the filament, NH fluorescence emission detected in the backward and side directions should give similar results. However, in our experiment, the on-axis backward NH fluorescence signal increases much faster (exponential increase) with the filament length than the one detected from the side (increase linearly). This indicates amplified spontaneous emission. By assuming that the intensity inside the filament is uniform because of intensity clamping [1-3], the gain coefficient (g) over the filament is obtained by fitting the experimental curve in Fig. 6.2(a) with $(e^{gL}-1)/g$ to get g=0.556 cm^{-1} [82]. We note that the value of gain from our measurement (0.556 cm^{-1} from NH) and that from [11] (0.300(3) cm^{-1} from N_2 for fluorescence measured at 357nm) are not comparable. The excited atomic nitrogen (N*) is essential for generating highly excited nitrogen monohydride radical (NH*), but there is no evidence that fragment N* is only from direct dissociation of excited molecular nitrogen (N_2*). For instance, it is possible that N_2 molecules are dissociated into fragments of atomic nitrogen (N) in ground state. After that the ground state fragments N are excited into N* by laser field or by collision. The polarization of the fluorescence from the backward and side direction is measured by rotating a polarizer placed just before the head of the fiber which couples to the ICCD. Both of them are randomly polarized as shown in Figs. 6.2 (c) and 6.2(d). The isotropic polarization and the difference between the gain in backward and side directions provide strong evidences for ASE lasing.

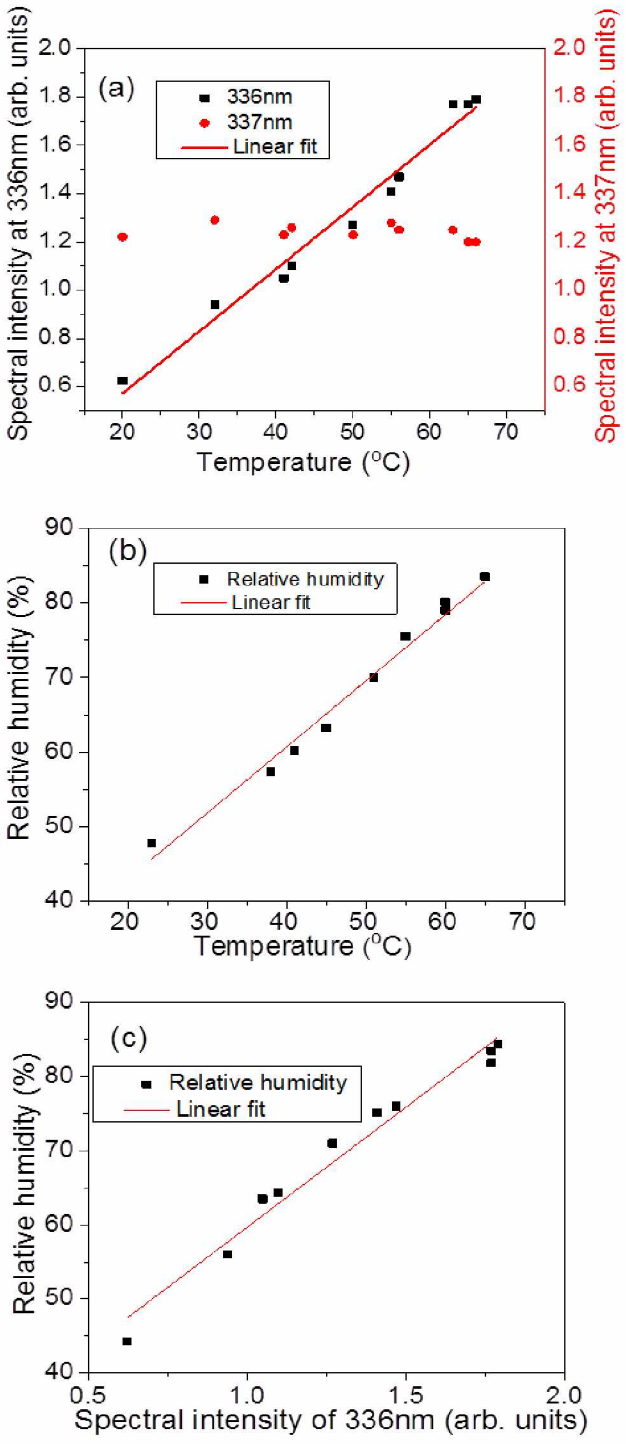

Fig. 6.3 (a) Fluorescence intensities of NH at 336 nm and N_2 at 337 nm versus the water temperature, with filament-to-water surface at 6 mm. (b) The relative humidity at 6 mm above the water surface versus the water temperature. The relative humidity is obtained from hygrometer. (c) The retrieved relative humidity by combining (a) and (b) as a function of the NH fluorescence signal at 336 nm.

In this sense, the ASE lasing testifies that the NH free radical, the product of filament-induced chemical reaction, is in an excited state and the population is inverted. Therefore, the translation of NH $A^3\Pi \rightarrow X^3\Sigma^-$ gives strong radiation at 336 nm, which can be used for the humidity measurement based on filament-induced spectroscopy since the fluorescence intensity from NH is dependent on the relative humidity. To calibrate the relative humidity, in Fig. 6.3(a) the fluorescence intensities of NH at 336 nm and N_2 at 337 nm were measured by varying the water temperature from 20°C to 66°C. The distance between the filament and the water surface was 6 mm. By increasing the water temperature, the NH fluorescence increases linearly, while the N_2 fluorescence keeps roughly constant. As a reference for humidity calibration, a hydrometer was fixed 6 mm above the water surface. The relative humidity was recorded by changing the water temperature and linearly fitted in Fig. 6.3(b). By combining the experimental curve in Fig. 6.3(a) and the reference in Fig. 6.3(b), we obtain the relative humidity as a function of NH fluorescence (Fig. 6.3(c)). The relative humidity is linearly proportional to the fluorescence signal of NH free radical. This result provides a significant way to measure relative humidity by monitoring NH fluorescence from filament-induced chemical reaction.

Thus, it is reasonable to conclude that the high intensity laser filament induced the dissociation of the nitrogen and water molecules. After that the collision of the highly excited fragments generates the excited NH free radical with population inversion. The strong emission at 336 nm occurs; it is sensitive to the number of water molecules in air. Besides, lasing action in NH radical means once we increase the length of the gain medium by increasing input pulse energy, it is expected to achieve stronger emission at 336 nm in backward direction. Remote humidity calibration needs to avoid influence from nonlinear dependence of NH fluorescence upon filament length. For this purpose, the fluorescence could be calibrated at a large angle, e.g. at 45° from backward direction. The strong fluorescence emission at 336 nm works as an effective approach for calibrating the humidity, even remotely.

6.4 Conclusion

In summary, strong fluorescence emission from NH free radical at 336 nm was observed in air. The fluorescence signal intensity is linearly dependent on the relative humidity around the filament region. The results reported in the paper not only give a further understanding of the filament-induced chemical reaction in air, but also open up possibilities to monitor the relative humidity remotely. The detailed underlying physics for the NH generation though filamentation awaits to be explored.

Chapter 7 Filamentation for atmospheric sensing

7.1 Introduction

Recent advances in high-intensity femtosecond laser technologies have made it possible to examine the spectral technique for identifying molecules with high sensitivity through femtosecond laser filamentation. Filamentation is accepted as a dynamic equilibrium between Kerr self-focusing and plasma-induced defocusing [1-6]. Due to the femtosecond pulse duration, which is short compared with the averaged electron collision time in air under normal atmospheric temperature and pressure condition, no inverse Bremstahlung and no cascade ionization are involved. Purely unimolecular multiphoton/tunnel ionization takes place. The plasma density ($\sim10^{14}$-10^{16} cm^{-3}) and temperature (5,800 K) are low in the filament plasma. A high intensity $\sim5\times10^{13}$ W/cm^2 is clamped inside a typical filament in air. Under this intensity in the femtosecond time scale, molecules, apart from being ionized, could be highly excited and dissociated, resulting in some “fingerprint” fluorescence of molecular fragments [41,42]. Thus, the states of molecules can be observed by using filament-induced fluorescence spectroscopy. Besides, the recent development in LIDAR (LIght Detection And Ranging) technique [27] could deliver the laser pulses over long distances and generates powerful filaments. Therefore the filament-induced fluorescence spectroscopy can be used for identifying various substances including chemical and biological species in the atmosphere ranging from gases and aerosols to solids [27, 86, 87, 94, 95].

Besides, due to its potential applications in remote sensing, research interests have been focused on how to enhance the filament-induced fluorescence emission, since stronger fluorescence enables us to detect targets from longer distances. The fluorescence can be enhanced by adjusting the initial laser parameters [1-6,129] or by using adaptive optics [27]. More recently by Xu et al, the filament-induced fluorescence signal from molecular N_2 has been enhanced when the second harmonic of the pump is incident together with the pump, because of two color excitation enhancement of ionization [130].

In this chapter, we investigate the fluorescence spectroscopy from a filament in air as a continuous CO_2 gas is blown into the filament. A series of spectral lines from the fragment CN transition $B\ ^2\Sigma - X\ ^2\Sigma$ are observed. This type of measurements could be further used for the measurement of the concentration of other molecules in air. Besides, by noncolinearly propagating and crossing two filaments in air, the fluorescence emission from the filament zone is enhanced.

7.2 Identification other molecules in air by filament-induced fluorescence spectroscopy

7.2.1 Experimental setup

The experiments were done by using a 6mJ/50fs, 1 kHz Ti:Sapphire laser beam. The schematic of the experimental setup is illustrated in Fig. 7.1. The laser beam passed through a BBO crystal for second harmonic generation, and was reflected by two dichroic mirrors (M1&M2) to filter out the remaining 800 nm pulses. After that, the beam was focused by a lens of 30 cm focal length. The pulse energy at 400 nm was 1.3 mJ (measured after the lens). A 2.5-cm-long filament was created in air. In order to increase the concentration of carbon dioxide (CO_2) around the filament region, a plastic box with open input and exit windows was installed to enclose the filament zone. A rectangular window was cut from the side for fluorescence detection. Inside the box, a gas nozzle, which continuously provided a CO_2 blow, was mounted beside the filament through a drilled hole. The fluorescence was detected from the side window at room temperature (20 ^{o}C).

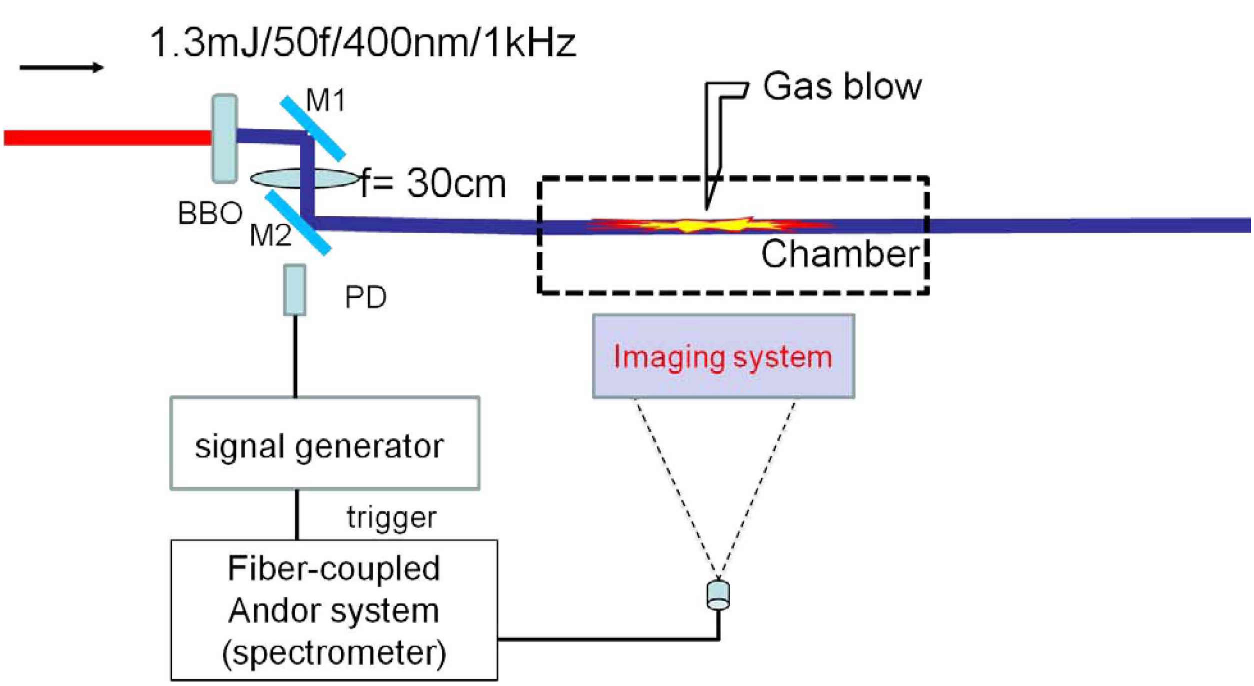

Fig 7.1 Schematic layout of the experimental setup

The fluorescence from the side was collected by an imaging system of 4 fused silica lenses, and sent to an ICCD-gated spectrometer (Andor Michelle M5000) through a fiber coupler. An external trigger was used in order to increase the signal-to-noise ratio. A photoelectric detector was placed after the mirror M2 to detect the leakage of the blue beam. The electric signal from the detector was then sent to a signal generator and amplified to 4.5 V (the external trigger of Andor system must be between 4.0-5.0 V). The output from the signal generator worked as the external trigger for the ICCD of the Andor Michelle M5000. The results were averaged over 100 000 laser shots.

7.2.2 Results and discussions

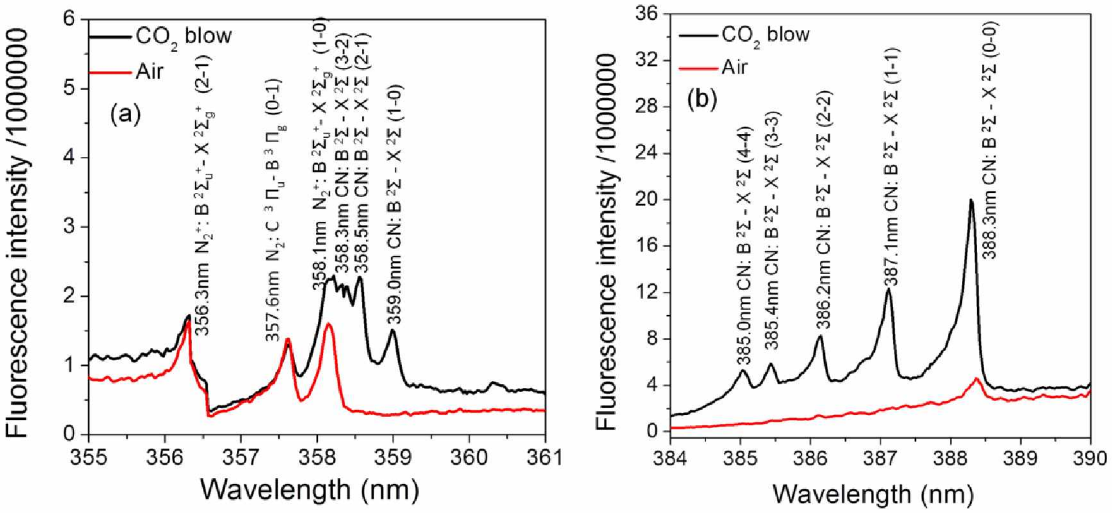

Fig.7.2 Typical spectrum in the range of 355–361 nm (a) and 384-390 nm (b) for filament-induced fluorescence of CN in air. The fluorescence was detected from the side at room temperature (20 °C).

"Clearn" fluorescence was found in the spectral range of 355-361 nm (a) and 384–390 nm (b). The filament-induced fluorescence in air with/without CO_2 blow is shown as the black/red curves in Fig. 7.2 respectively. In Fig 7.2, a series of spectral lines from CN radical's $B^2\Sigma$ - $X^2\Sigma$ transition were observed [see Table 7.1]. When we increased the flow of the CO_2 gas, the intensity of CN fluorescence became stronger. The generated CN radical was ascribed to the chemical reaction between N_2 and CO_2 molecules. The intense laser field induced the dissociation of N_2 and CO_2 molecules. The dissociated fragments then recombined with each other to create CN radicals. Since the concentration of molecular CO_2 in air was too low (~0.03%) to generate much CN radicals, from the red curve in Fig. 7.2(a, b), only spectral lines from N_2 could be found. In the case of blowing CO_2, which directly increased the amount of molecular CO_2 in air, more CN radicals were created. The new generated CN radicals were at an excited state, thus, emitting a series of fluorescence.

Table 7.1 Details of the observed lines. All data are taken from [116].

Peaks	Originality		Transition		Intensity
Wavelength (nm)	element		v’	v’’	
356.3	N_2^+	$B\ ^2\Sigma_u^+ - X\ ^2\Sigma_g^+$	2	1	9
357.6	N_2	$C\ ^3\Pi_u - B\ ^3\Pi_g$	0	1	10
358.1	N_2^+	$B\ ^2\Sigma_u^+ - X\ ^2\Sigma_g^+$	1	0	9
358.3	CN	$B\ ^2\Sigma - X\ ^2\Sigma$	3	2	6
358.5	CN	$B\ ^2\Sigma - X\ ^2\Sigma$	2	1	7
359.0	CN	$B\ ^2\Sigma - X\ ^2\Sigma$	1	0	8
385.0	CN	$B\ ^2\Sigma - X\ ^2\Sigma$	4	4	4
385.4	CN	$B\ ^2\Sigma - X\ ^2\Sigma$	3	3	6
386.2	CN	$B\ ^2\Sigma - X\ ^2\Sigma$	2	2	8
387.1	CN	$B\ ^2\Sigma - X\ ^2\Sigma$	1	1	9
388.3	CN	$B\ ^2\Sigma - X\ ^2\Sigma$	0	0	10

Similar to the relative humidity measurement by using the fluorescence from NH radical in chapter 6 [83], the concentration of CO_2 could be measured by measuring the fluorescence intensity of CN. Although we have not done any quantitative measurements by varying the concentration of CO_2, those ideas could be our next step after this thesis and might have some further applications.

The fluorescence life time of the excited state of $CN : B\ ^2\Sigma - X\ ^2\Sigma\ (0-0)$ emitting fluorescence at 388.3 nm is shown in Fig. 7.3. During the measurements, we manually scanned the gate delay at the ICCD spectrometer with gate width of 2 ns. The time “0” was set by the ICCD spectrometer. As shown in Fig. 7.3, the fluorescence emission from $CN : B\ ^2\Sigma - X\ ^2\Sigma\ (0-0)$

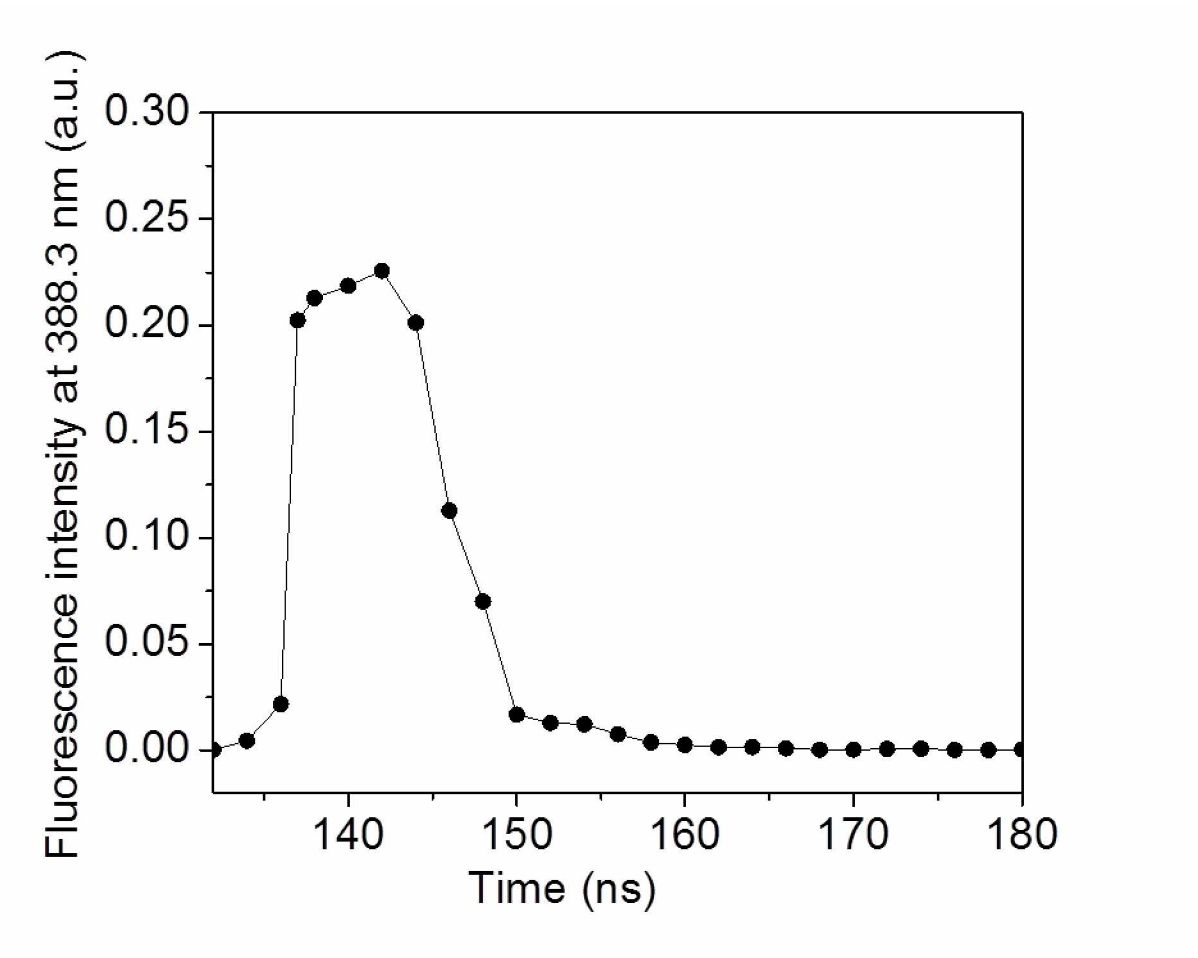

Fig. 7.3 Fluorescence decay of the excited state $CN: B\ ^2\Sigma - X\ ^2\Sigma\ (0-0)$

rapidly increased around the time delay at ~137 ns. Strongest fluorescence emission from CN radical could be observed between 137-144 ns. After that, it gradually decayed within ~20 ns. The fluorescence life time which is induced by fs laser filament is much shorter than that caused by ns pulse, which is in μs timescale [141].

7.3 Fluorescence enhancement by noncollinear interaction of femtosecond filaments:

Inside a single infrared filament, the intensity is clamped to $\sim 5\times10^{13}$ W/cm^2 in air [1-6]. However, if we non-collinearly overlap two or more filaments in air, a plasma grating will be created [52, 56, 131-138], which strongly enhances the local field intensity beyond the clamped intensity limit. In order to investigate the fluorescence enhancement, we try to detect the fluorescence intensity from the interaction region of two filaments.

7.3.1 Experimental setup

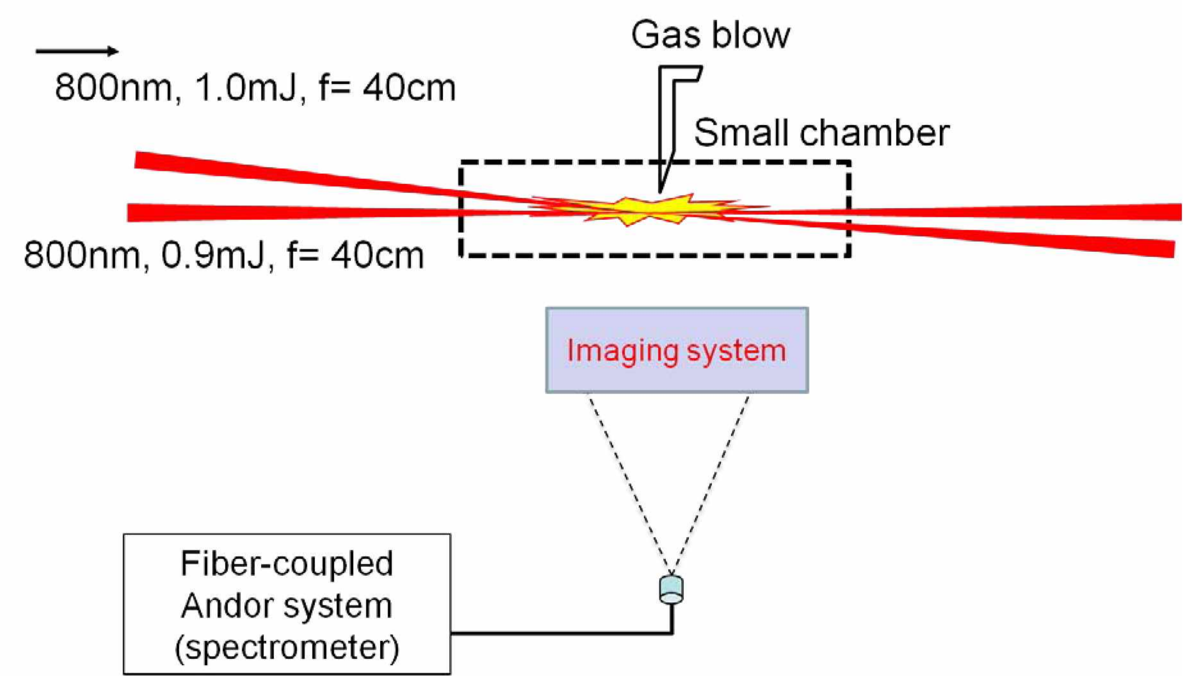

Fig 7.4 Schematic layout of the experimental setup for fluorescence detection

The schematic of the experimental set up is shown in Fig. 7.4. The filaments were generated by two pulses with pulse energy and duration of 1.0 mJ/ 50fs and 0.9 mJ/50 fs. The two pulses with the same polarization were focused to produce two non-collinearly crossed filaments using separate lenses with the same focal length of 40 cm. As a result, two crossed filaments about ~1.5 cm in length were produced as the two pulses propagated individually. The time delay between the two filaments was modulated by a delay stage. In our experiment, the crossing angle between the two filaments was fixed at 7.0°. The fluorescence detection system and the small chamber for blowing CO_2 in Fig. 7.4 were similar to the previous setup in Fig. 7.1. This time we did not use an external trigger for the ICCD spectrometer. The spectra were taken under continuous CO_2 blow and integrated over 100 s (100 000 shots).

7.3.2 Results and discussion

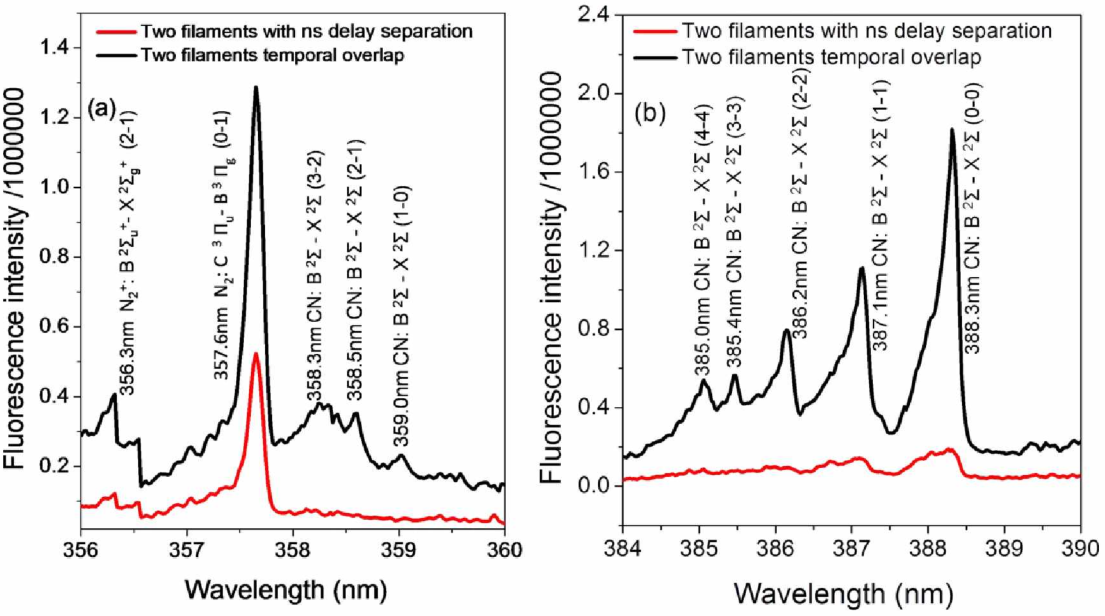

Fig.7.5 Typical spectra in the range of 356-360 nm (a) and 384-390 nm (b) for the fluorescence of CN with continuous CO_2 blow. The black curves were taken when the two infrared filaments were temporally overlapped, while the red curves were measured when there was a ~2 ns time delay between the two infrared filaments.

Under continuous CO_2 blow, the two infrared filaments with the same polarization and incident pulse energy of 1.0 mJ and 0.9 mJ were crossed. We carefully adjusted the time delay between the two filamenting pulses to avoid any influence from molecular alignment. It was set at ~2 ns. In this case, there was no strong interaction between the two filaments. The filament-induced spectra were recorded as the red curves in Fig. 7.5(a, b). The spectral lines from CN radicals were rather weak, even if there was "something" a round 388.3 nm, which possibly indicated CN radical from $B\ ^2\Sigma - X\ ^2\Sigma\ (0-0)$. We also tried to measure the fluorescence emission as the two infrared filamenting pulses propagated individually. The spectral lines from CN radicals could not be identified as well.

However, once the two non-collinearly crossed infrared filaments temporally overlapped, a "brighter" plasma channel was produced indicating larger electron/ion density. The black curves in Fig. 7.5 (a,b) were taken when the plasma channel was the "brightest". In this case, "clean" fluorescence of CN radicals from $B\ ^2\Sigma - X\ ^2\Sigma$ transition was found. The following gives an explanation of the observation.

When the two non-collinearly crossed infrared filaments were temporally overlapped, the local field intensity increased in the overlapping region (plasma grating) where constructive interference occurred [122, 131-133]. Due to the mutiphoton/tunnel ionization of air molecules was a highly nonlinear process, more molecules would ionize in this region, even if the intensity increased a little bit. The intensity at the plasma grating was measured to be ~$1.2*10^{14}$ W/cm^2 in [139], which was stronger than that in a single free propagating infrared filament (~5×10^{13} W/cm^2 [1,139]). Higher intensity inside the plasma grating stimulated stronger nonlinear optical processes. Under CO_2 blow, the dissociation of molecular CO_2 and N_2 was more probable to occur. It produced more fragments of C and N. The dissociated fragments recombined with each other to create more CN radicals, resulting in stronger fluorescence emission of CN$(B\ ^2\Sigma - X\ ^2\Sigma\ \ transition)$.

In the case of two filaments temporally separated by ~ 2 ns, there was no interaction between the two filaments. The local field intensity was not enhanced to produce more CN radicals. Thus, the fluorescence intensity from two crossed filaments with temporal separation of ~2 ns was similar to the summation of the fluorescence intensity from each individual filament. Therefore the spectral lines of CN from the red curves in Fig.7.5 (a,b) were rather weak.

Besides, the higher intensity inside the plasma grating also increased the multiphoton/tunnel ionization of neutral nitrogen, creating more excited N_2^{+*} [71]. The first negative band system of excited N_2^{+*} at 356.3 nm was thus enhanced as compared to the case of the filaments temporally separated by ~2ns (Fig. 7.5 (a)). Also, the following recombination $N_2 + N_2^+ \rightarrow N_4^+$ was followed by $N_4^+ + e \rightarrow N_2^*(C\ ^3\Pi_u) + N_2$ [41,42,88]. More molecule in state $N_2^*(C\ ^3\Pi_u)$ were generated. Therefore the emission from the second positive band system $(C\ ^3\Pi_u - B\ ^3\Pi_g\ \ transition)$ of N_2 at 357.6nm was also enhanced (Fig. 7.5 (a)) as compared to the case of non-temporally overlapping filaments.

7.4 Conclusion

We experimentally investigate the fluorescence spectroscopy as continuous CO_2 gas blow is applied to a filament. A series of spectral lines from the excited fragments of

CN ($B\ ^2\Sigma - X\ ^2\Sigma$) were observed. Such filament-induced fluorescence spectroscopy could be used to measure the concentration of other molecules in air. Besides, the filament-induced fluorescence could be enhanced during the non-collinear interaction of two filaments, which provided an opportunity for more efficient atmospheric sensing.

Chapter 8 Conclusion

In this thesis, we have experimentally investigated the filamentation induced nonlinear optics during the propagation of a femtosecond laser pulse in atomic/molecular gases. When an intense femtosecond laser pulse propagates in air, the dynamic equilibrium between Kerr self-focusing and plasma defocusing creates the filament. A high intensity to $\sim 5 \times 10^{13}$ W/cm^2 is clamped inside a filament over a long distance, which induces a lot of nonlinear processes, including: atomic/molecular birefringence, amplified spontaneous emission, the chemical reactions and the filament induced fluorescence spectroscopy, etc.

We did a lot of pump-probe experiments in order to investigate of the detailed polarization states of an output probe pulse in atomic/molecular gas. In an atomic gas, when the probe pulse was synchronized with an infrared filament (chapter 3), by retrieving the phase delay using the rotation angle of the main axis of the probe, the birefringence inside a filament was measured. In a molecular gas, the polarization rotation for the main axis of a probe pulse at the revival of molecular N_2 was experimentally analyzed. The rotation angle of the probe pulse was modulated by the revival of molecular N_2 (chapter 4). This polarization rotation of the probe which induced by whatever Kerr effect in atomic gases or Raman effect at molecular revival, could be used in polarization gating which is important of information processing.

Furthermore, filament emits “fingerprint” fluorescence. The “clean” fluorescence from a filament provides information of detailed molecular states. By investigating the fluorescence from a filament in backward and side directions, the fluorescence emission from radicals OH (chapter 5) and NH (chapter 6) can be found. The backscattered fluorescence from both OH and NH show an exponential increase with increasing filament length, indicating amplified spontaneous emission. We also gave a brief explanation for the dissociation and recombination processes for the creation of radicals OH and NH at excited states. Actually, it is the first experimental result that the lasing action in water vapor and NH are found in air.

Finally, the plasma grating which is generated by non-colinearly overlapping two filaments was supposed to enhance the local field intensity beyond the clamped intensity limit (chapter 7). A series of spectral lines from the excited fragments of CN was found when continuous CO_2 gas blow was applied to the overlapping region of non-colinearly overlapped two filaments (plasma grating). Same phenomenon could not be observed, when each filament propagated individually. It means the high intensity inside the plasma can be potentially used in femtosecond pulse induced chemical reactions.

It is hoped that the study presented in this thesis will be helpful to the comprehension of the filamentation phenomenon. There are still many challenging questions needed to be clarified in future research; for instance, what is the detailed physical picture in the chemical reaction for generation NH and CN, whether we can make use of the fluorescence from CN radicals to calibrate the concentration of CO_2 or CO, etc. To fit different potential requirements, the topic for “filamentation induced nonlinear optics” will become even hotter in the near future.

Bibliography

1. S. L. Chin, Femtosecond Laser Filamentation, Vol. 55 of Springer Series on Atomic, Optical and Plasma Physics (Springer, 2010).

2. A. Couairon and A. Mysyrowicz, Femtosecond filamentation in transparent media, Phys. Rep. 441, 47 (2007).

3. S. L. Chin, The physics and the challenge of the propagation of powerful femtosecond laser pulses in optical media, Physics in Canada, 60, 273 (2004).

4. L. Bergé, S. Skupin, R. Nuter, J. Kasparian, J.P. Wolf, Supercontinuum emission and enhanced self-guiding of infrared femtosecond filaments sustained by third-harmonic generation in air, Rep. Prog. Phys. 70, 1633 (2007).

5. J. Kasparian and J. P. Wolf, Physics and applications of atmospheric nonlinear optics and filamentation, Opt. Express 16, 466 (2008).

6. S.L. Chin, S.A. Hosseini, W. Liu, Q. Luo, F. Théberge, N. Aközbek, A. Becker, V.P. Kandidov, O.G. Kosareva, and H. Schroeder, The propagation of powerful femtosecond laser pulses in optical media: physics, applications, and new challenges, Canadian Journal of Physics, 83, 905 (2005)

7. R.Y. Chiao, E. Garmire, and C.H. Townes. Self-trapping of optical beams, Phys. Rev. Lett. 13, 479 (1964).

8. J.H. Marburger, Self-focusing: Theory, Prog. Quantum Electron, 4, 35 (1975).

9. D. Strickland and G. Mourou, Compression of amplified chirped optical pulses, Opt. Commun. 56, 219 (1985).

10. D. E. Spence, P. N. Kean, and W. Sibbett, 60-fsec Pulse Generation from a Self-mode-locked Ti:sapphire Laser, Opt. Lett. 16, 42 (1991).

11. Q. Luo, W. Liu, and S. L. Chin, Lasing action in air induced by ultrafast laser filamentation, Appl. Phys. B 76, 337 (2003).

12. W. Liu and S. L. Chin, Direct measurement of the critical power of femtosecond Ti:sapphire laser pulse in air, Optics Express, 13, 5750 (2005).

13. A. Braun, G. Korn, X. Liu, D. Du, J. Squier, and G. Mourou, Self-channeling of high-peak-power femtosecond laser pulses in air, Opt. Lett. 20, 73 (1995).

14. J. Kasparian, M. Rodriguez, G. Méjean, J. Yu, E. Salmon, H. Wille, R. Bourayou, S. Frey, Y.B. André, A. Mysyrowicz, R. Sauerbrey, J.P. Wolf, and L. Wöste, White-light filaments for atmospheric analysis, Science 301, 61 (2003).

15. V. I. Talanov, Focusing of light in cubic media, JETP Lett. 11, 199 (1970).

16. S. L. Chin, T. J. Wang, C. Marceau, J. Wu, J. S. Liu, O. Kosareva, N. Panov, Y. P. Chen, J. F. Daigle, S. Yuan, A. Azarm, W. W. Liu, T. Saideman, H. P. Zeng, M. Richardson, R. Li, and Z. Z. Xu, Advances in Intense Femtosecond Laser Filamentation in Air, Laser Phys. 22, 1 (2012).

17. J.F. Daigle, O. Kosareva, N. Panov, M. Bégin, F. Lessard, C. Marceau, Y. Kamali, G. Roy, V.P. Kandidov, and S.L. Chin, A simple method to significantly increase filaments\257 length and ionization density, Appl. Phys. B., 94, 249, (2009).

18. F. Théberge, N. Aközbek, W.W. Liu, A. Becker, and S.L. Chin, Tunable Ultrashort Laser Pulses Generated through Filamentation in Gases, Phys. Rev. Lett. 97, 023904 (2006).

19. J. Kasparian, R. Sauerbrey, and S.L. Chin, The critical laser intensity of self-guided light filaments in air, Appl. Phys. B 71, 877 (2000).

20. H. Cai, J. Wu, Y. Peng, and H. Zeng, Comparison study of supercontinuum generation by molecular alignment of N_2 and O_2, Opt. Express 17, 5822 (2009).

21. S. Varma, Y. H. Chen, and H. M. Milchberg, Trapping and destruction of long-range high-intensity optical filaments by molecular quantum wakes in air, Phys. Rev. Lett. 101, 205001 (2008).

22. P. F. Lu, J. Liu, H. Li, H. F. Pan, J. Wu and H. P. Zeng, Cross-correlation frequency-resolved optical gating by molecular alignment for ultraviolet femtosecond pulse measurement, Appl. Phys. Lett. 97, 061101 (2010)

23. R. R. Alfano, "The Supercontinuum Laser Source" Springer-Verlag, New York (1989).

24. G. Heck, E. J. Judge, J. Odhner, M. Plewicki, and R. J. Levis, Remote sensing via femtosecond filament based technologies, GomacTech Digest Conference, Orlando, FL, Presented (2009).

25. D. Mirell, O. Chalus, K. Peterson, and J. C. Diels, Remote sensing of explosive using infrared and ultraviolet filaments, J. Opt. Soc. Am. B, 25, B108 (2008).

26. H. L. Xu, G. Méjean, W. Liu, Y. Kamali, J. F. Daigle, A. Azarm, P. T. Simard, P. Mathieu, G. Roy, J.-R. Simard, S.L. Chin, Remote sensing of similar biological materials using femtosecond filament-induced breakdown spectroscopy, Applied Physics B, 87, 151 (2007).

27. J. F. Daigle, Y. Kamali, M. Châteauneuf, G. Tremblay, F. Théberge, J. Dubois, G. Roy, and S.L. Chin, Remote sensing with intense filaments enhanced by adaptive optics, Appl. Phys. B., 97, 701 (2009).

28. J. Kasparian, R. Ackermann, Y.B. André, G. Méchain, G. Méjean, B. Prade, P. Rohwetter, E. Salmon, K. Stelmaszczyk, J. Yu, A. Mysyrowicz, R. Sauerbrey, L. Wöste, and J. P. Wolf, Electric events synchronized with laser filaments in thunder clouds, Opt. Express 16, 5757 (2008).

29. X. S. Zhang, A. Lytle, T. Popmintchev, X. B. Zhou, H. C. Kapteyn and M. M. Murnane, and O. Cohen, Quasi-phasematching and quantum path control of high-harmonic generation using counterpropagating light, Nature Physics 3, 270 (2007).

30. C. D. Amico, A. Houard, M. Franco, B. Prade, A. Mysyrowicz, A.Couairon, and V. T. Tikhonchuk, Conical forward THz emission from femtosecond-laser-beam filamentation in air, Phys. Rev. Lett. 98, 235002 (2007).

31. X. Xie, J.M. Dai, and X.C. Zhang, Coherent control of THz wave generation in ambient air, Phys. Rev. Lett. 96, 075005 (2006).

32. T.J. Wang, S. Yuan, Y. Chen, J.F. Daigle, C. Marceau, F. Théberge, M. Châteauneuf, J. Dubois, and S. L. Chin, Toward remote high energy terahertz generation, Appl. Phys. Lett. 97, 111108 (2010).

33. Y. Liu, A. Houard, B. Prade, S. Akturk, A. Mysyrowicz, and V.T. Tikhonchuk, Terahertz radiation source in air based on bifilamentation of femtosecond laser pulses, Phys. Rev. Lett. 99, 135002 (2007).

34. J. Liu, J.M Dai, S. L. Chin and X.C. Zhang, Broadband terahertz wave remote sensing using coherent manipulation of fluorescence from asymmetrically ionized gases, Nature Photonics 4, 631 (2010).

35. F. Theberge, M. Châteauneuf, G. Roy, P. Mathieu, and J. Dubois, Generation of tunable and broadband far-infrared laser pulses during two-color filamentation, Phys. Rev. A 81, 033821 (2010).

36. Y. Chen, C. Marceau, S. Génier, F. Théberge, M. Châteauneuf, J. Dubois and S.L. Chin, Elliptically polarized Terahertz emission through four-wave mixing in a two-color filament in air, Opt. Comm.282, 4283 (2009).

37. T.J. Wang, S. Yuan, Y. P. Chin and S. L. Chin, Intense broadband THz generation from femtosecond laser filamentation, Chin. Opt. Lett. 11, 011401 (2013).

38. T.J. Wang, H. L. Xu, J. F. Daigle, A. Sridharan, S. Yuan, and S. L. Chin, Water vapor concentration measurement in air using filament-induced fluorescence spectroscopy, Opt. Lett. 37, 1706 (2012).

39. T.J Wang, J.F Daigle, S. Yuan, F. Théberge, M. Châteauneuf, J. Dubois, G. Roy, H. Zeng and S. L. Chin, Remote generation of high-energy terahertz pulses from two-color femtosecond laser filamentation in air, Phys. Rev. A 83, 053801 (2011).

40. H. Yang, J. Zhang, J. Zhang, L. Z. Zhao, Y. J. Li, H. Teng, Y. T. Li, Z. H. Wang, Z. L. Chen, Z. Y. Wei, J. X. Ma, W. Yu, and Z. M. Sheng, Third-order harmonic generation by self-guided femtosecond pulses in air, Rev. E 66, 05401 (2002).

41. S.L. Chin, H.L. Xu, Q. Luo, F. Théberge, W. Liu, J.F. Daigle, Y. Kamali, P.T. Simard, J. Bernhardt, S.A. Hosseini, M. Sharifi, G. Méjean, A. Azarm, C. Marceau, O. Kosareva, V.P. Kandidov, N. Aközbek, A. Becker, G. Roy, P. Mathieu, J.R. Simard, M. Châteauneuf, and J. Dubois, Filamentation "remote" sensing of chemical and biological agents/pollutants using only one femtosecond laser source, Appl. Phys. B, 95, 1 (2009).

42. H.L. Xu, and S. L. Chin, Femtosecond laser filamentation for atmospheric sensing, Sensors 11, 32 (2011).

43. H. Cai, J. Wu, A. Couairon, and H. Zeng, Spectral modulation of femtosecond laser pulse induced by molecular alignment revivals, Opt. Lett. 34, 827 (2009).

44. J.Wu, H. Cai, A. Couairon, and H. Zeng, Wavelength tuning of a few-cycle laser pulse by molecular alignment in femtosecond filamentation wake, Physical Review A 79, 063812 (2009).

45. V. Renard, M. Renard, S. Guérin, Y. T. Pashayan, B. Lavorel, O. Faucher, and H. R. Jauslin, Postpulse molecular alignment measured by a weak field polarization technique, Phys. Rev. Lett. 90, 153601 (2003).

46. J. Wu, H. Cai, Y. Peng, and H. Zeng, Controllable supercontinuum generation by the quantum wake of molecular alignment, Phys. Rev. A 79, 041404(R) (2009).

47. Y. H. Feng, W. X. Li, J. Liu, H.F. Pan, J. Wu, and H. P. Zeng, Direct retrieval of Kerr and plasma effects from alignment-induced spatiotemporal modulation, Opt. Lett. 37, 3746 (2012).

48. F. Rosca-Pruna and M. J. J. Vrakking, Experimental observation of revival structures in picosecond laser-induced alignment of I_2, Phys. Rev. Lett. 87, 153902 (2001).

49. R. A. Bartels, T. C. Weinacht, N. Wagner, M. Baertschy, C. H. Greene, M. M. Murnane, and H. C. Kapteyn, Phase modulation of ultrashort light pulses using molecular rotational wave packets, Phys. Rev. Lett. 88, 013903 (2001).

50. H. Cai, J. Wu, H. Li, X. Bai, and H. Zeng, Elongation of femtosecond filament by molecular alignment in air, Opt. Express 17, 21060 (2009).

51. X. Yang, J. Wu, Y. Peng, Y. Tong, S.Yuan, L. Ding, Z. Xu, and H. Zeng, Noncollinear interaction of femtosecond filaments with enhanced third harmonic generation in air, Appl. Phys. Lett. 95, 111103 (2009).

52. X. Yang, J. Wu, Y. Tong, L. Ding, Z. Xu, and H. Zeng, Enhancement of third harmonic generation by a laser-induced plasma, Appl. Phys. Lett. 97, 071108 (2010).

53. H.P. Zeng, P. Lu, J. Liu, and W.X. Li, in "Progress in Ultrafast Intense Laser Science VIII"Kaoru Yamanouchi ed., Springer, ISBN 978 -3-642-28725-1 (2012).

54. T. Fuji, T. Suzuki, E. E. Serebryannikov, and A. Zheltikov, Experimental and theoretical investigation of *a* multicolor filament, Phys. Rev. A 80, 063822 (2009).

55. L. P. Shi, W. X. Li, H. Zhou, D. Wang, L. E. Ding, Enhanced ultraviolet pulse generation via dual-color filament interaction induced phase-matching control, Appl. Phys. Lett. 102, 081112 (2013).

56. L.P. Shi, W.X. Li, Y.D. Wang, X. Lu, L. Ding, and H. P. Zeng, Generation of high-density electrons based on plasma grating induced Bragg diffraction in air, Phys. Rev. Lett. 107, 095004 (2011).

57. Robert W. Boyd, Nonlinear Optics, second edition (Academic Press, New York (2003).

58. G. P. Agrawal, "Highly Nonlinear Fibers and Their Applications" Institute of optics university of Rochester, Rochester NY 14627 (2007).

59. T. J. Wang, "Recent progress on filamentation nonlinear optics at Laval University", Presentation in Jilin University, Jilin Changchun China 130000 (2013).

60. S. Petit, A. Talebpour, A. Proulx, S.L. Chin, Some consequences during the propagation of an intense femtosecond laser pulse in transparent optical media: a strongly deformed white-light laser, Laser Physics, 10, 100 (2000).

61. A. Talebpour, J. Yang and S. L. Chin, Semi-empirical model for the rate of tunnel ionization of N_2 and O_2 molecule in an intense Ti:Sapphire laser pulse, Opt. Commun. 162, 29 (1999).

62. W. Liu, F. Théberge, E. Arévalo, J. F. Gravel, A. Becker and S. L. Chin, Experiment and simulations on the energy reservoir effect in femtosecond light filaments, Opt. Lett. 30, 2602 (2005).

63. S. L. Chin, From Multiphoton to Tunnel Ionization, From Multiphoton to Tunnel Ionization, in Advances in Multiphoton Processes and Spectroscopy, edited by S. H. Lin, A. A. Villaeys and Y. Fujimura, World Scientific, Singapore 16, 249 (2004).

64. H. Stapelfeldt and T. Seideman, Colloquium: Aligning molecules with strong laser pulses, Rev. Mod. Phys. 75, 543 (2003).

65. C. Marceau, S. Ramakrishna, S. Génier, T. Wang, Y. Chen, F. Théberge, M. Châteauneuf, J. Dubois, T. Seideman and S. L. Chin, Femtosecond filament induced birefringence in argon and in air: Ultrafast refractive index change, Opt. Comm. 283, 2732 (2010).

66. S. Yuan, T. J. Wang, O. Kosareva, N. Panov, V. Makarov, H. P. Zeng and S. L. Chin, Measurement of birefringence inside a filament, Phys. Rev. A 84, 013838 (2011).

67. S. L. Chin, "Fundamentals of Laser Optoelectronics" Vol 1, World Scientific Publishing Co., Singapore (1989), pp. 170.

68. C. Marceau, Y. Chen, F. Théberge, M. Châteauneuf, J. Dubois, and S. L. Chin, Ultrafast birefringence induced by a femtosecond laser filament in gases, Opt. Lett. 34, 1419 (2009).

69. P. R. Hemmer, R. B. Miles, P. Polynkin, T. Siebert, A. V. Sokolov, P. Sprangle, and M. O. Scully, Standoff spectroscopy via remote generation of a backward-propagating laser beam, Proc. Natl. Acad. Sci. U.S.A. 108, 3130 (2011).

70. D. Kartashov, S. Ališauskas, A. Pugzlys, A. Baltuška, M. Shneider, and A. Zheltikov, Free-space nitrogen laser from a mid-infrared filament, research in Optical Sciences, OSA Technical Digest, HW3C.2 (2012).

71. S. L. Chin, H. L. Xu, Y. Cheng, Z. Z. Xu and K. Yamanouchi, Natural population inversion in a gaseous molecular filament, Chin. Opt. Lett. 11, 013201 (2013).

72. M. N. Shneider, A. Baltuska, and A. M. Zheltikov, Population inversion of molecular nitrogen in an Ar: N_2 mixture by selective resonance-enhanced multiphoton ionization, J. Appl. Phys.110,083112 (2011).

73. J. Penano, P. Sprangle, B. Hafizi, D. Gordon, R. Fernsler and M. Scully, Remote lasing in air by recombination and electron impact excitation of molecular nitrogen, J. Appl. Phys. 111, 033105 (2012).

74. S. Owada, A. Azarm, S. Hosseini, A. Iwasaki, S. L. Chin and K. Yamanouchi, Amplified spontaneous $C_3\Pi_u$-$B_3\Pi_g$ emission and rotational and vibrational state distributions in $C_3\Pi_u$ state of N_2 in femtosecond laser induced filament in air, Chem. Phys. Lett. 581 21 (2013).

75. H. Zhang, C. Jing, J. Yao, G. Li, B. Zeng, W. Chu, J. Ni, H. Xie, H. L. Xu, S. L. Chin, K. Yamanouchi, Y. Cheng, and Z. Z. Xu, Rotational coherence encoded in an "air-laser" spectrum of nitrogen molecular ions in an intense laser field, Phys. Rev. X 3 041009 (2013).

76. J. Yao, G. Li, C. Jing, B. Zeng, W. Chu, J. Ni, H. Zhang, H. Xie, C. Zhang, H. Li, H. L. Xu, S. L. Chin, Y. Cheng, and Z. Z. Xu, Remote creation of coherent emissions in air with two-color ultrafast laser pulses, New J. Phys. 15 023046 (2013).

77. J.P. Yao, B. Zeng, H.-L. Xu, G.-H. Li, W. Chu, J.-L. Ni, H.-S. Zhang, S. L. Chin, Y. Cheng, and Z.Z. Xu, High-brightness switchable multiwavelength remote laser in air, Phys. Rev. A 84, 051802 (2011).

78. W. Chu, G. H. Li, H. Q. Xie, J. L. Ni, J. P. Yao, B. Zeng, H. S. Zhang, C. R. Jing, H. L. Xu, Y. Cheng, and Z. Z. Xu, A self-induced white light seeding laser in a femtosecond laser filament, Laser Physics Letters 11, 015301 (2014).

79. Y. Cheng, J.L. Ni, W. Chu, H. S. Zhang, B. Zeng, J. P. Yao, G. Li, C. R. Jing, H. Q Xie, H. L. Xu, Z. Z. Xu, and L. L. Qiao, Impulsive rotational Raman scattering of N_2 by a remote “air laser” in femtosecond laser filament, Opt. Lett., 39, 2250 (2014).

80. J. L. Ni, W. Chu, C. R. Jing, H. S. Zhang, B. Zeng, J. P. Yao, G. H. Li, H. Q. Xie, C. J. Zhang, H. L. Xu, S. L. Chin, Y. Cheng, and Z. Z. Xu, Identification of the physical mechanism of generation of coherent N_2^+ emissions in air by femtosecond laser excitation, Opt. Exp. 21, 8746 (2013).

81. J. L. Ni, W. Chu, H.S. Zhang, C.R. Jing, J.P. Yao, H.L. Xu, B. Zeng, G. Li, C. Zhang, S. L. Chin, Y. Cheng and Z.Z. Xu, Harmonic-seeded remote laser emissions in N_2-Ar, N_2-Xe and N_2-Ne mixtures: a comparative study, Opt. Exp. 20, 20970 (2012).

82. S. Yuan, T. J. Wang, Y. Teranishi, A. Sridharan, S. H. Lin, H. P. Zeng and S. L. Chin, Lasing action in water vapor induced by ultrashort laser filamentation, Appl. Phys. Lett. 102 224102 (2013).

83. S. Yuan, T.J. Wang, P.F. Lu, S. L. Chin and H. P. Zeng, Humidity measurement in air using filament-induced nitorgen monohydride fluorescence spectroscopy, Appl. Phys. Lett. 104 091113 (2014).

84. W. Chu, H.L. Li, J.L Ni, B. Zeng, J.P. Yao, H.S. Zhang, G. Li, C. Jing, H. Xie, H.L. Xu, K. Yamanouchi, and Y. Cheng, Lasing action induced by femtosecond laser filamentation in ethanol flame for combustion diagnosis Appl. Phys. Lett 091106 (2014).

85. S. Hosseini, A. Azarm, J. F. Daigle, Y. Kamali and S. L. Chin, Filament-induced amplified spontaneous emission in air-hydrocarbons gas mixture, Opt. Comm. 316 61 (2014).

86. S. Morel, N. Leone, P.Adam, J. Amouroux, Detection of bacteria by time-resolved laser-induced breakdown spectroscopy, Appl. Opt. 42, 6191 (2003).

87. W.B. Lee, J.Y. Wu, Y.I. Lee, J.Sneddon, Recent applications of laser-induced breakdown spectrometry: a review of material approaches, Appl. Spectrosc. Rev., 39, 97 (2004).

88. H.L. Xu, A. Azarm, J. Bernhardt, Y. Kamali, and S.L. Chin, The mechanism of nitrogen fluorescence inside a femtosecond laser filament in air, Chem. Phys.360, 171 (2009).

89. F. Théberge, W.W Liu, P.T. Simard, A. Becker, S. L. Chin, Plasma density inside a femtosecond laser filament in air: Strong dependence on external focusing, Physical Review E, 74, 036406 (2006).

90. J. Bernhardt, W. Liu, F. Théberge, H.L. Xu, J.F. Daigle, M. Châteauneuf, J. Dubois and S.L. Chin, Spectroscopic analysis of femtosecond laser plasma filament in air, Optics Communications, 280, 1268 (2008).

91. S.L. Chin, A. Brodeur, S. Petit, O.G. Kosareva & V.P. Kandidov, Filamentation and supercontinuum generation during the propagation of powerful ultrashort laser pulses in optical media (white light laser), Journal of Nonlinear Optical Physics and Materials, 8, 146 (1999).

92. G. Méjean, J. Kasparian, J. Yu, S. Frey, E. Salmon, R. Ackermann, J.P. Wolf, L.Bergé, S. Skupin, UV–Supercontinuum generated by femtosecond pulse filamentation in air: Meter-range experiments versus numerical simulations, Appl. Phys. B, 83, 345 (2006).

93. F. Théberge, W. Liu, Q. Luo, S.L. Chin, Ultrabroadband continuum generated in air (down to 230 nm) using ultrashort and intense laser pulses, Appl. Phys. B, 80, 225 (2005).

94. J.F. Daigle, Y. Kamali, G. Roy, and S.L. Chin, Remote filament-induced fluorescence spectroscopy from thin clouds of smoke, Appl. Phys. B, 93, 759 (2008).

95. A. Talebpour, M. Abdel-Fattah, A. D. Bandrauk and S. L. Chin, Spectroscopy of the gases interacting with intense femtosecond laser pulses, Laser Physics, 11, 76 (2001).

96. F. Théberge, "Third-order parametric processes during the filamentation of ultrashort laser pulses in gas" Thesis for doctorate (2007).

97. L. Berge, and S. Skupin, Few-cycle light bullets created by femtosecond filaments, Phys. Rev. Lett. 100, 113902 (2008).

98. Y.R. Shen, "The principles of Nonlinear Optics", John Wiley&Sons, New York, (1984), pp. 28 and 286-301.

99. P. Béjot, Y. Petit, L. Bonacina, J. Kasparian, M. Moret and J.P. Wolf, Ultrafast gaseous "half-wave plate", Opt. Express 16 7564 (2008).

100. Y. Chen, C. Marceau, F. Théberge, M. Châteauneuf, J. Dubois, and S. L. Chin, Polarization separator created by a filament in air, Opt. Lett. 33, 2731 (2008).

101. F. Calegari, C. Vozzi, S. Gasilov, E. Benedetti, G. Sansone, M. Nisoli, S. De Silvestri, and S.Stagira, Rotational Raman effects in the wake of optical filamentation, Phys. Rev. Lett. 100, 123006 (2008).

102. O. Kosareva, N. Panov, V. Makarov, I. Perezhogin, C. Marceau, Y.-P Chen, S. Yuan, T. J. Wang, H. P. Zeng, A. Savel'ev and S. L. Chin, Polarization rotation due to femtosecond filamentation in an atomic gas, Opt. Lett. 35, 2904 (2010).

103. A. Bernstein, M. McCormick, G. Dyer, J. Sanders, and T. Ditmire, Two-beam coupling between filament-forming beams in air, Phys. Rev. Lett. 102, 123902 (2009).

104. N. Tang and R. L. Sutherland, Time-domain theory for pump–probe experiments with chirped pulses, J. Opt. Soc. Am. B 14, 3412 (1997).

105. L. Bergé, S. Skupin, and G. Steinmeyer, Temporal self-restoration of compressed optical filaments, Phys. Rev. Lett. 101, 213901 (2008).

106. V. Renard, O. Faucher, and B. Lavorel, Measurement of laser-induced alignment of molecules by cross defocusing, Opt. Lett. 30, 70 (2005).

107. J. Wu, H. Cai, Y.Q. Tong, and H.P. Zeng, Measurement of field-free molecular alignment by cross-defocusing assisted polarization spectroscopy, Opt. Express, 17,16300 (2009).

108. J. Wu, H. Cai, Y. Peng, Y.Q. Tong, A. Couairon, and H.P. Zeng, Control of femtosecond filamentation by field-free revivals of molecular alignment, Laser Phys. 19, 1759 (2009).

109. J. Itatani, J. Levesque, D. Zeidler, H. Niikura, H. Pépin, J. Kieffer, P. Corkum, and D. Villeneuve, Tomographic imaging of molecular orbitals, Nature London 432, 867 (2004).

110. J.F. Ripoche, G. Grillon, B. Prade, M. France, E. Nibbering , R. Lange, and A. Mysyrowicz, Determination of the time dependence of n_2 in air, Opt. Commun. 135, 310 (1997).

111. J. Wu, H. Qi, and H. Zeng, Extreme-ultraviolet frequency combs by surface-enhanced optical fields with diatomic molecules, Phys. Rev. A 77, 053412 (2008).

112. M. B. Gaarde and A. Couairon, Intensity Spikes in Laser Filamentation: Diagnostics and Application, Phys. Rev. Lett. 103 043901 (2009).

113. D.S. Steingrube, E. Schulz, T. Binhammer, M. B. Gaarde, A. Couairon, U. Morgner and M. Kovačev, High-order harmonic generation directly from a filament New Journal of Physics, 13 043022 (2011).

114. F. Théberge, N. Aközbek, W. Liu, J. Filion, and S.L. Chin, Conical emission and induced frequency shift of third-harmonic generation during ultrashort laser filamentation in air, Optics Communications, 275, 298, (2007).

115. A. Dogariu, J. B. Michael, M. O. Scully, and R. B. Miles, High gain backward lasing in air, Science 331, 442 (2011).

116. R. W. B. Pearse and A. G. Gaydon, The Identification of Molecular Spectra, 4th ed, page 264-265 (Chapman & Hall, 1976).

117. L. C. Lee, OH yield from H_2O photodissociation in 1050–1370 Å. J. Chem. Phys. 72, 4334 (1980).

118. O. Dutuit, A. TabcheFouhaile, I. Nenner, H. Frohlich, and P.M. Guyon, Photodissociation processes of water vapor below and above the ionization potential, J. Chem. Phys. 83, 584 (1985).

119. L. C. Lee, L. Oren, E. Phillips and D. L. Judge, Cross sections for production of the OH fluorescence by photodissociation of H_2O vapour, J. Phys. B: Atom. Molec. Phys. 11, 47 (1978).

120. S. Q. Xu, X. Sun, B. Zeng, W. Chu, J. Zhao, W. Liu, Y. Cheng, Z. Z. Xu, and S. L. Chin, Simple method of measuring laser peak intensity inside femtosecond laser filament in air, Opt. Express 20, 299 (2012).

121. S. Tsurubuchi, Correlation diagrams for electronic states of H2O and fragment species, Chem. Phys. 10, 335 (1975).

122. P.F. Lu, J. Wu, and H.P. Zeng, Manipulation of plasma grating by impulsive molecular alignment, Appl Phys. Lett. 103, 221113 (2013).

123. A. Azarm, D. Song, K. Liu, S. Hosseini, Y. Teranishi, S. H. Lin, A. Xia, F.A. Kong and S. L. Chin, Neutral dissociation of hydrogen molecules in a strong laser field through superexcited states, J. Phys. B: At. Mol. Opt. Phys. 44, 085601 (2011).

124. T.J. Wang, J.J. Ju, J.F. Daigle, S. Yuan, R.X. Li and S. L. Chin, Self-seeded forward lasing action from a femtosecond Ti:sapphire laser filament in air, Laser Phys. Lett. 10 125401 (2013).

125. H. Li, H.L. Xu, B.S. Yang, Q.D. Chen, T. Zhang, and H.B. Sun, Sensing combustion intermediates by femtosecond filament excitation, Opt. Lett. 38, 1250 (2013).

126. Y. Petit, S. Henin, J. Kasparian, and J.P. Wolf, Production of ozone and nitrogen oxides by laser filamentation, Appl. Phys. Lett. 97, 021108 (2010).

127. P. Rohwetter, J. Kasparian, K. Stelmaszczyk, Z. Hao, S. Henin, N. Lascoux, W. M. Nakaema, Y. Petit, M. Queißer, R. Salamé, E. Salmon, L. Wöste, J.P. Wolf, Laser-induced water condensation in air, Nat. Photonics 4, 451 (2010).

128. J. J. Ju, J.S. Liu, C. Wang, H.Y. Sun, W.T. Wang, X.C. Ge, C. Li, S. L. Chin, R.X. Li, and Z. Z. Xu, Laser-filamentation-induced condensation and snow formation in a cloud chamber, Opt. Lett. 37, 1214 (2012).

129. T.J. Wang, Y. Chen, C. Marceau, F. Théberge, M. Châteauneuf, J. Dubois and S.L. Chin, High energy terahertz emission from two-color laser-induced filamentation in air with pump pulse duration control, Appl. Phys. Lett. 95, 131108 (2009).

130. H. L. Xu, A. Azarm, and S. L. Chin, Controlling fluorescence from N_2 inside femtosecond laser filaments in air by two-color laser pulses, Appl. Phys. Lett. 98, 141111 (2011).

131. H. Wu, T. Yang, Y.Wang, and L. Ding, Background-free third-order harmonic generation induced by dynamic gratings in dual filaments, J. Opt. Soc. Am. B 26, 645 (2009).

132. X. Yang, J. Wu, Y. Peng, Y. Tong, P. Lu, L. Ding, Z. Xu, and H. Zeng, Plasma waveguide array induced by filament interaction, Opt. Lett. 34, 3806 (2009).

133. L.P Shi, W.X. Li,, D.B. Bai, H. Zhou, D. Wang, L. Ding, and H.P. Zeng, Enhanced fluorescence emission of helium atoms by seeded optically driven impact excitation, Phys Rev. A. 88, 013418 (2013).

134. S. Suntsov, D. Abdollahpour, D.G. Papazoglou, and S.Tzortzakis, Femtosecond laser induced plasma diffraction gratings in air as photonic devices for high intensity laser applications, Appl. Phys. Lett. 94, 251104 (2009).

135. Z. Liu, P. Ding, Y. Shi, X. Lu, S. Sun, X. Liu, Q. Liu, B. Ding, and B. Hu, Control of third harmonic generation by plasma grating generated by two noncollinear IR femtosecond filaments, Opt. Express 20, 8837 (2012).

136. J. Liu, W.X. Li, H. Li, Y. Feng, H. Pan, J. Wu, and H.P. Zeng, Comparison of frequency-resolved optical polarization gating induced by molecular alignment and Kerr effects, Opt. Lett. 37, 2748 (2012).

137. J. Liu, P.F. Lu, Y. Tong, H. Pan, X. Yang, J. Wu, and H.P. Zeng, Two-dimensional plasma grating by noncollinear femtosecond filament interaction in air, Appl. Phys. Lett. 99, 151105 (2011).

138. J. Liu, Y. Feng, H. Li, P. Lu, H. Pan, J. Wu, and H.P. Zeng, Supercontinuum pulse measurement by molecular alignment based cross-correlation frequency resolved optical gating, Opt. Express 19, 40 (2011).

139. J. Liu, thesis for doctorate "Femtosecond laser filamentation interaction and characterization" East China Normal University, Shanghai, China 200062 (2012).

140. A Talebpour, M. Abdel-Fattah, S.L. Chin, Focusing limits of intense ultrafast laser pulses in a high pressure gas: road to new spectroscopic source, Optics Communications, 183, 484 (2000).

141. D. A. Cremers and L. J. Radziemski, Handbook of laser-induced breakdown spectroscopy, Chichester, John Wiley & Sons (2006).

List of publications and presentations

Publications

1. **S. Yuan**, T. J. Wang, Y. Teranishi, A. Sridharan, S. H. Lin, H. P. Zeng and S. L. Chin, "Lasing action in water vapor induced by ultrashort laser filamentation", Appl. Phys. Lett. 102 224102 (2013).

2. **S. Yuan**, T. J. Wang, O. Kosareva, N. Panov, V. Makarov, H. P. Zeng and S. L. Chin, "Measurement of birefringence inside a filament", Phys. Rev. A 84, 013838 (2011).

3. **S. Yuan**, T. J. Wang, H. P. Zeng and S. L. Chin, "Humidity measurement in air using filament-induced NH fluorescence spectroscopy", Appl. Phys. Lett. 104 091113 (2014)

4. **S. Yuan**, S. L. Chin, and H.P. Zeng, "Femtosecond Filamention Induced Fluorescence Technique for Atmospheric Sensing" submitted to Chin. Phys. B

5. **S. Yuan**, T. J. Wang, H. P. Zeng and S. L. Chin, "Polarization Evolution of a probe pulse in the wake of molecular alignment inside a filament", to be submitted.

6. T. J Wang, **S. Yuan**, Y. Chen, J. F Daigle, C. Marceau, F. Théberge, M. Châteauneuf, J. Dubois, and S. L. Chin, "Toward remote high energy terahertz generation", Appl. Phys. Lett. 97, 111108 (2010).

7. T. J. Wang, **S. Yuan**, Y. P. Chin and S. L. Chin "Intense broadband THz generation from femtosecond laser filamentation", Chin. Opt. Lett. 11, 011401 (2013).

8. T. J. Wang, **S. Yuan**, Z. D. Sun, C. Marceau, Y. Chen, F. Théberge, M. Châteauneuf, J. Dubois, and S. L. Chin, "Molecular alignment control of terahertz emission from a two-color filament in air", Laser Phys. Lett. 8, 295 (2011).

9. T. J Wang, J. F Daigle, **S. Yuan**, F. Théberge, M. Châteauneuf, J. Dubois, G. Roy, H. Zeng and S. L. Chin, "Remote generation of high-energy terahertz pulses from two-color femtosecond laser filamentation in air", Phys. Rev. A 83, 053801 (2011).

10. T. J. Wang, C. Marceau, **S. Yuan**, Y. Chen, Q. Wang, F. Théberge, M. Châteauneuf, J. Dubois, and S. L. Chin, "External focusing effect on terahertz emission from a two-color femtosecond laser-induced filament in air", Laser Phys. Lett. 8, 57 (2011).

11. T. J Wang, C. Marceau, Y. Chen, **S. Yuan**, F. Théberge, M. Châteauneuf, J. Dubois, and S. L. Chin, "THz emission from a dc-biased two-color femtosecond laser-induced filament in air", Appl. Phys. Lett. 96, 211113 (2010).

12. J. F. Daigle, T. J. Wang, S. Hosseini, **S. Yuan**, G. Roy and S. L. Chin, “Dynamic behavior of postfilamentation Raman pulses”, Appl. Opt. 50, 6234 (2011).

13. J. F. Daigle, F. Théberge, M. Henriksson, T. J. Wang, **S. Yuan**, M. Châteauneuf, J. Dubois, M. Piché and S. L. Chin, “Remote THz generation from two-color filamentation: long distance dependence”, Opt. Express 20, 6825 (2012).

14. O. Kosareva, J. F Daigle, N. Panov, T. J Wang, S. Hosseini, **S. Yuan**, G. Roy, V. Makarov, and S. L. Chin, “Arrest of self-focusing collapse in femtosecond air filaments: higher order Kerr or plasma defocusing”, Opt. Lett. 36, 1035 (2011).

15. T.-J. Wang, H. L. Xu, J. F. Daigle, A. Sridharan, **S. Yuan**, and S. L. Chin, “Water vapor concentration measurement in air using filament-induced fluorescence spectroscopy”, Opt. Lett. 37, 1706 (2012).

16. O. Kosareva, N. Panov, V. Makarov, I. Perezhogin, C. Marceau, Y. P Chen, **S. Yuan**, T.J. Wang, H. P. Zeng, A. Savel'ev and S. L. Chin, “Polarization rotation due to femtosecond filamentation in an atomic gas”, Opt. Lett. 35, 2904 (2010).

Presentations

1. **S. Yuan**, S. L. Chin, H. P. Zeng “Humidity measurement in air using filament-induced NH fluorescence spectroscopy” the filamentation Workshop on “Strong Field Laser Science” Shanghai, China, Nov. 2013.